

predicting phase transition mechanisms by integrating atomistic simulations, experiments, and AI techniques



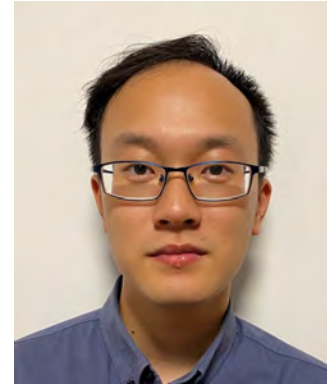
Lijie He, PhD



Haomin Liu, PhD



Ali Shargh, PhD



Zhaotong Du, MS

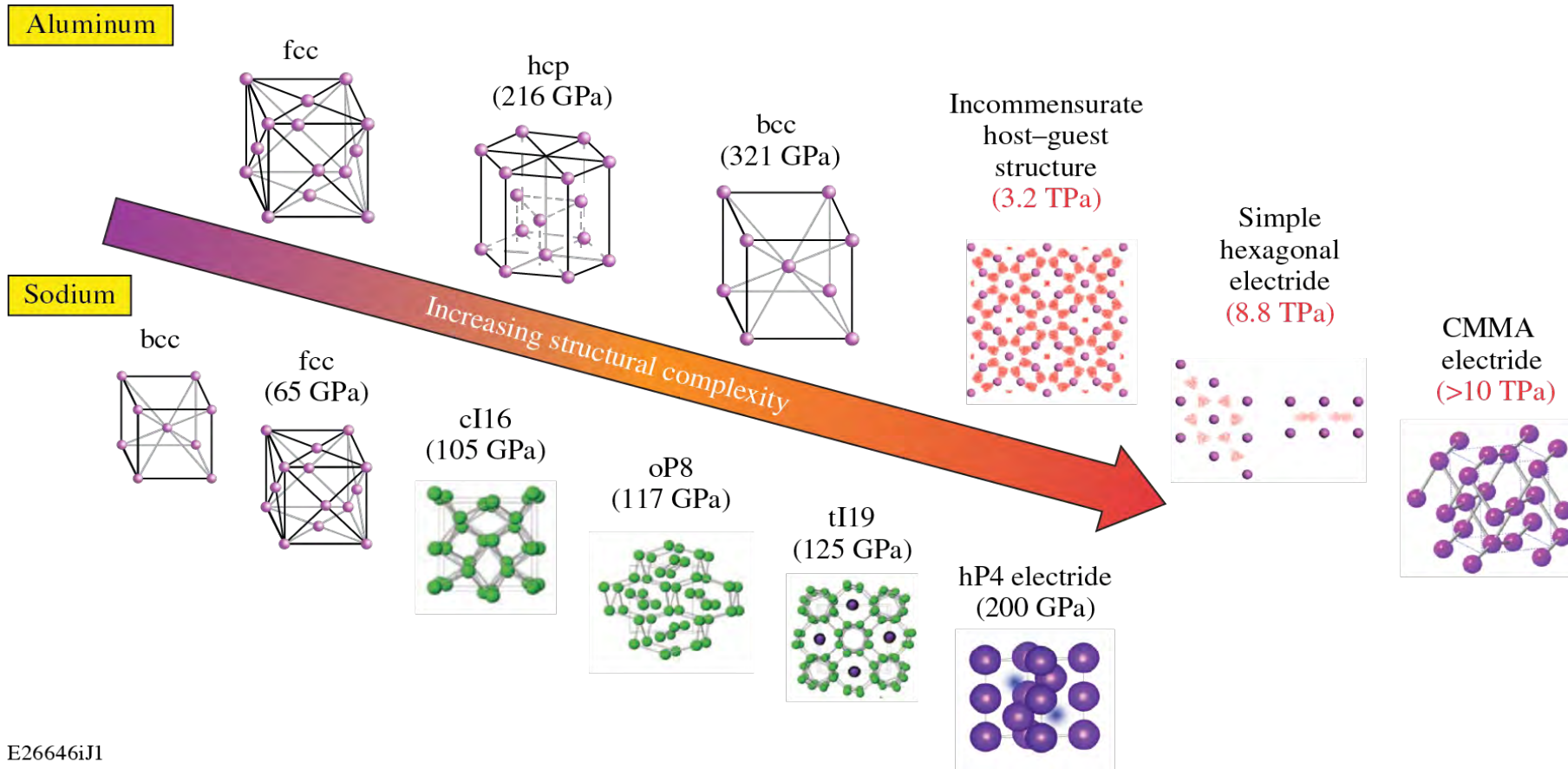


Jerardo Salgado, PhD

Niaz Abdolrahim
LLNL, 2022



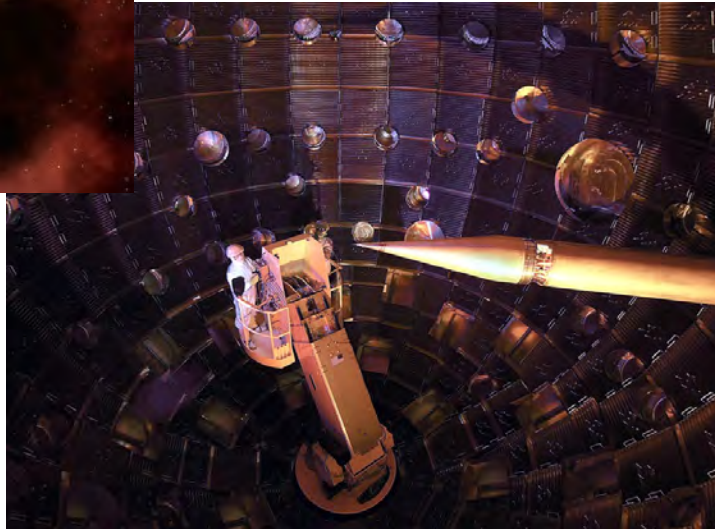
Materials at High-Energy-Density (HED)



Understanding materials at HED



[How are planets form](#)



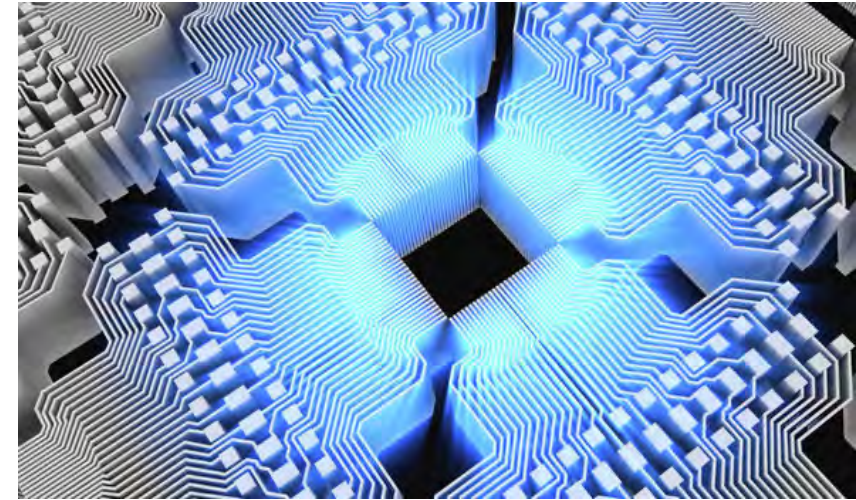
Cheap energy created from fusion and delivered over superconducting wires

[National Ignition Facility experiment puts researchers at threshold of fusion ignition](#)



Quest for room temperature superconductivity

[Room-temperature superconductivity](#)



Superfast quantum computers

[IBM supercomputer](#)



HED capabilities in the U.S. and worldwide.

Facility/End Station	Type of Machine	Energy Delivered	Peak Power	Repetition Rate	Maximum Pressures	Key physics goals
National Ignition Facility	Laser	1.8-MJ UV photons	500 TW	~1 shot/ 3 h	to 10 TPa	New physics of H and simple elements to atomic pressure
Z	Pulsed power	3.5-MJ current	350 TW/ 26 MA	~1 shot/ day	0.5 TPa	Elements and matter beyond Thomas–Fermi
OMEGA/ OMEGA EP	Lasers	30-kJ UV	30 TW	~1 shot/ 3 h	1 TPa	New techniques for dense H and matter beyond Thomas–Fermi
Matter at Extreme End Station (LCLS)	X-ray laser	1-mJ x rays + 50-J laser	10 GW	120 Hz	0.3 TPa	Unwrapping complex structures and kinetic pathways to complexity
Dynamic Compression Sector (APS)	Laser, guns, x ray	1- μ J x rays + 100-J laser	10 MW	120 Hz	0.3 TPa	Unwrapping complex structures for mid-to-high Z
Laser Net	Lasers	to 20 kJ	to 30 TW	Several	1 TPa	Develop structure and electronic property techniques
Diamond-Anvil Cell Facilities (including APS and BNL)	Static compression x ray, THz	NA	NA	Continuous	0.5 TPa	Understand kinetic thresholds and constrain ground states



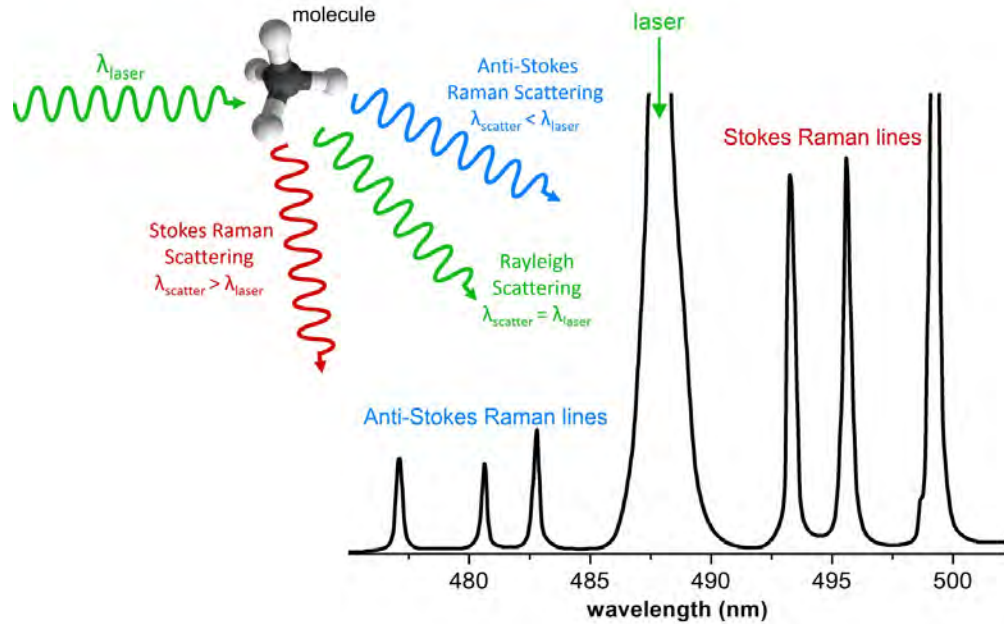
To explore the multiscale nature of matter from atomic to the macro-scale, connecting experimental observations with atomistic simulations and deep learning computer vision techniques to answer key question of how atomic rearrangement through defect motion enables the bulk phase transformations in extreme solids

Outline

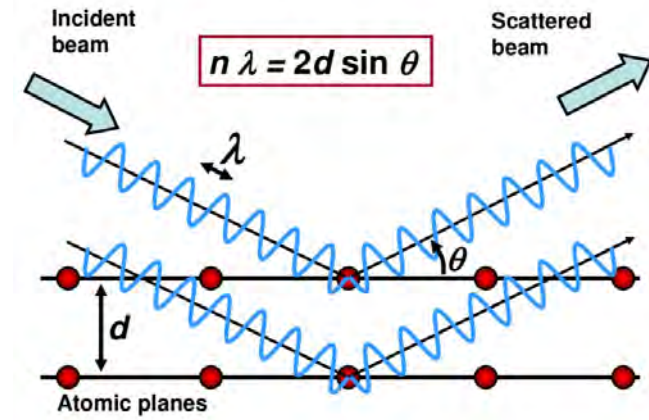
- Phase transformation of Aluminum at high pressure (XRD analysis)
- Phase identification of water at ambient temperature (Raman, IR, and XRD analysis)
- Developing AI-powered models for classification of large XRD data



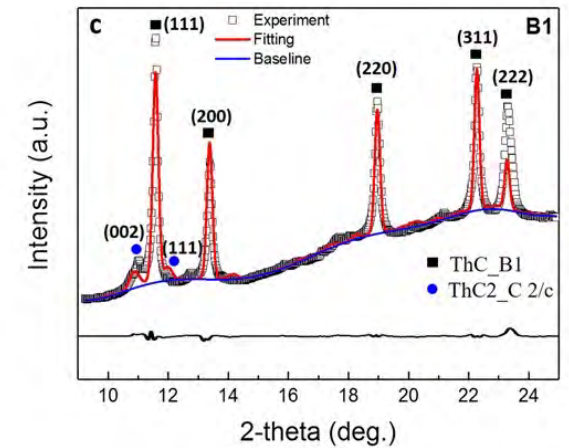
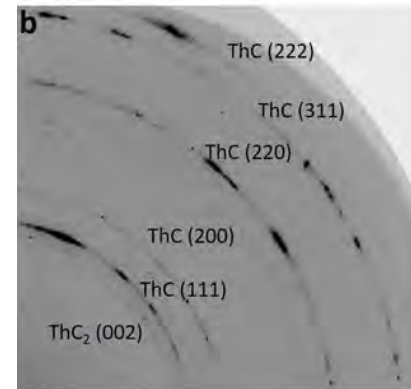
Crystal structure diagnostics



[Principles of Raman spectroscopy](#)



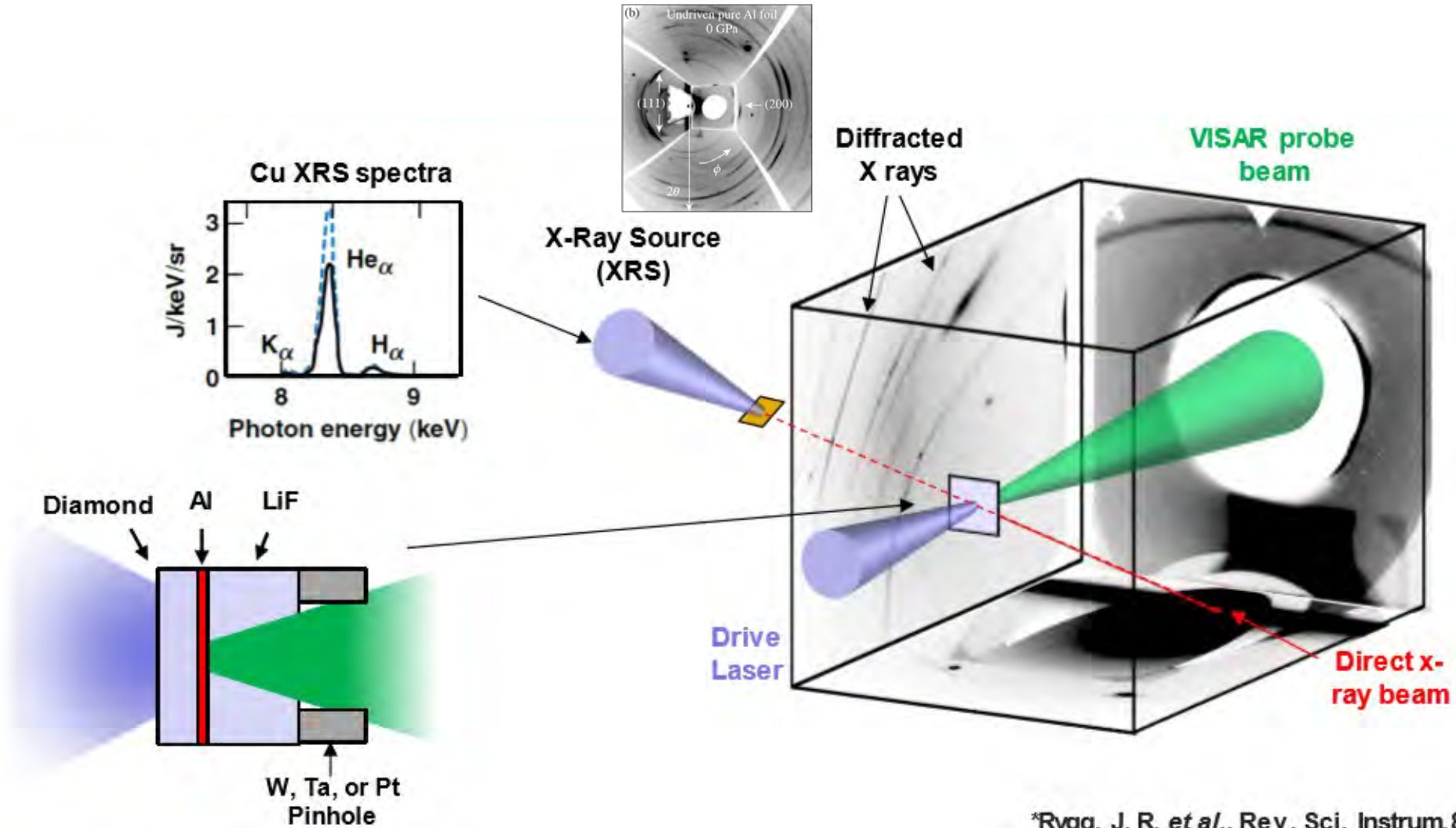
[Principles of X-ray diffraction](#)



[XRD of Thorium monocarbide](#)



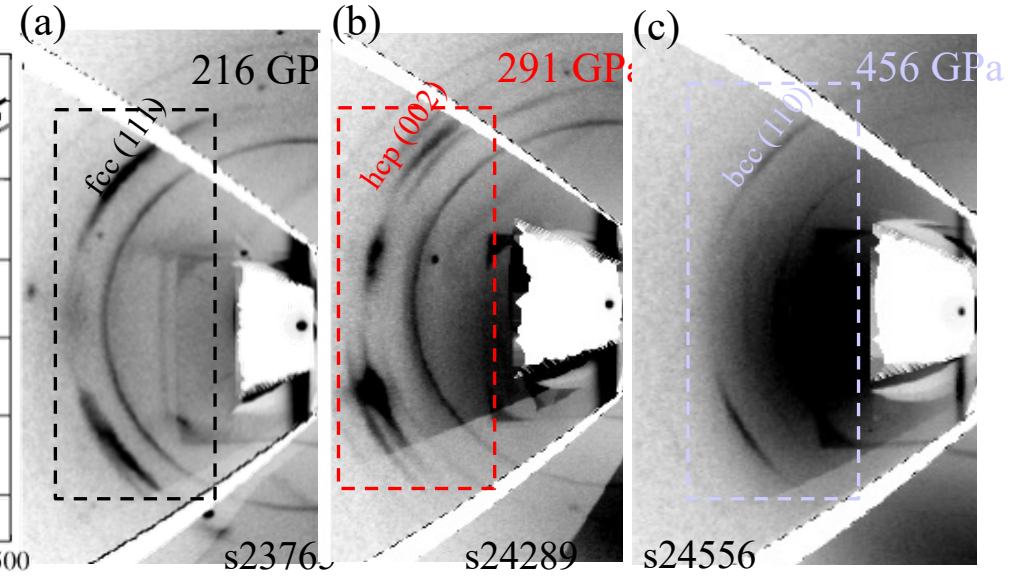
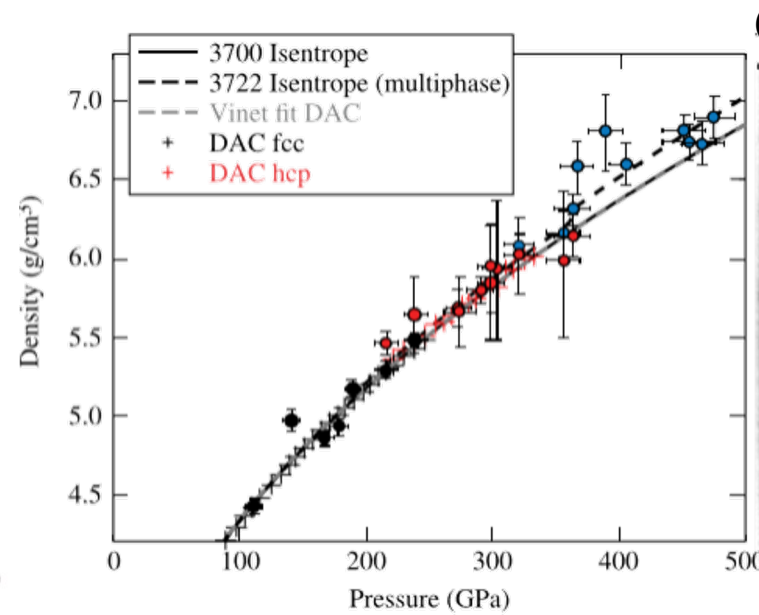
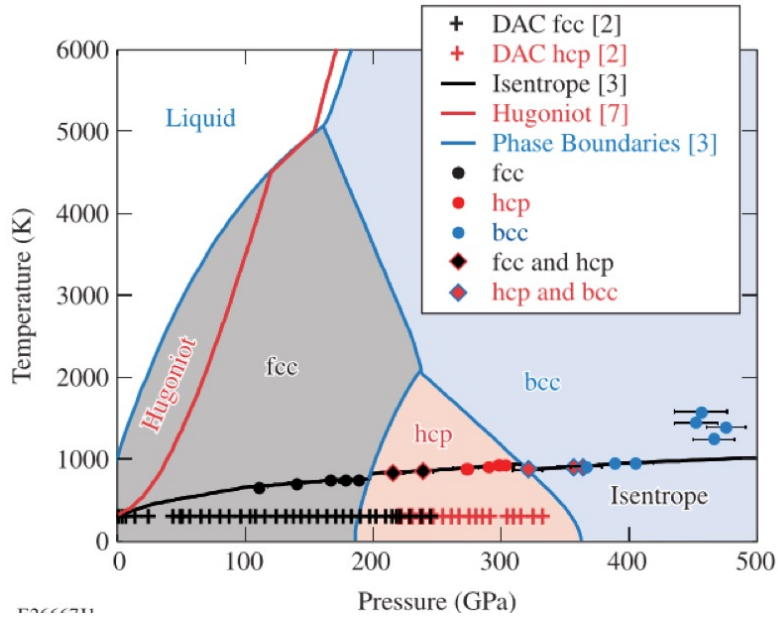
Phase transformation of Aluminum-Ramp compression loading



*Rygg, J. R. *et al.*, Rev. Sci. Instrum. **83**, 113904 (2012)



Phase transformation of Aluminum- Experimental observations

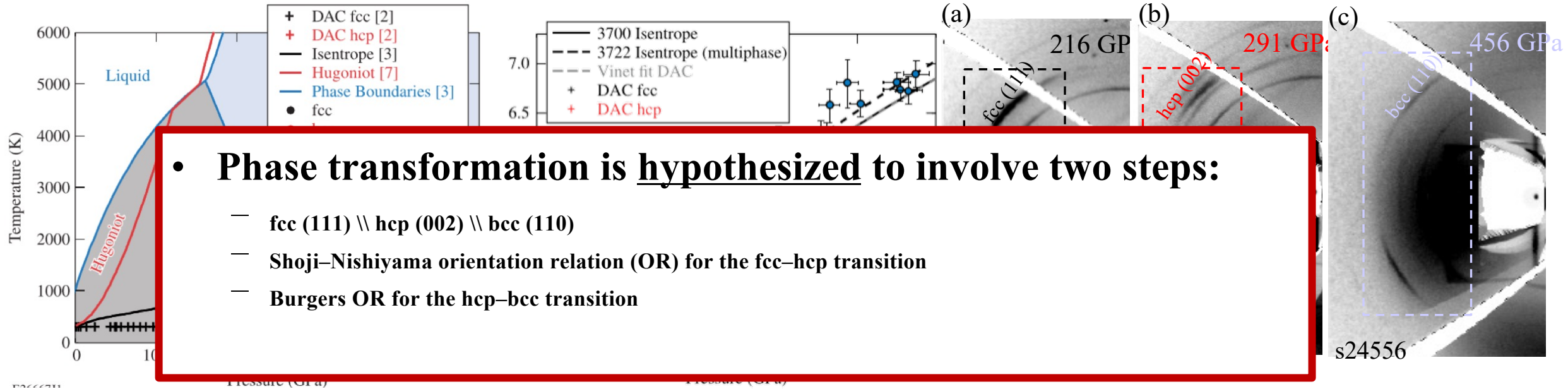


*Polsin, D. N. et al., Phys. Plasmas 25, 082709 (2018)

- Stress-density response follows Al isentrope
- In situ XRD show fcc-hcp-bcc phase transformation



Phase transformation of Aluminum- Experimental observations

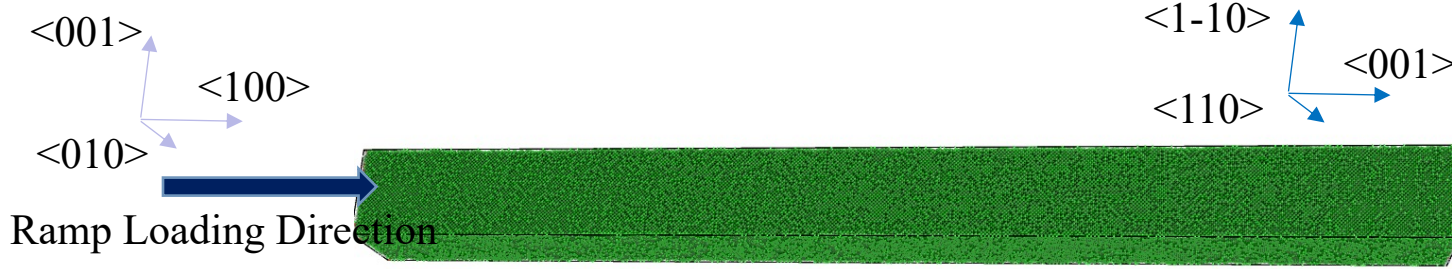


*Polsin, D. N. et al., Phys. Plasmas 25, 082709 (2018)

- Stress-density response follows Al isentrope
- In situ XRD show fcc-hcp-bcc phase transformation



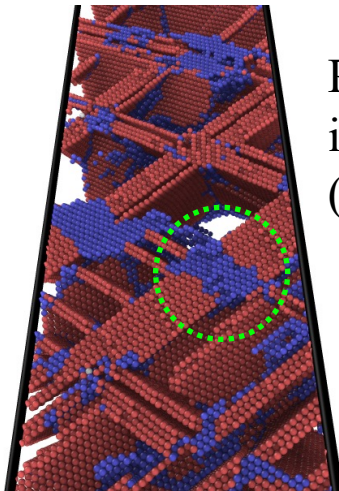
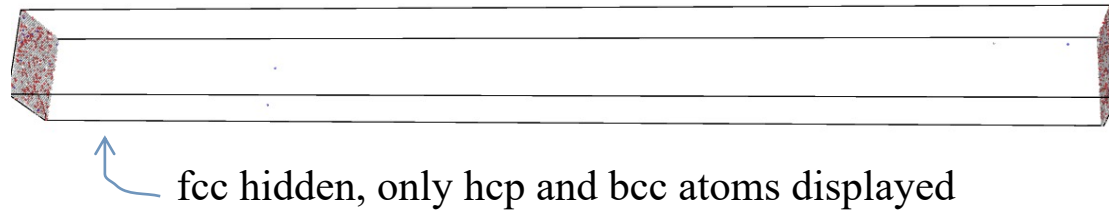
Phase transformation of Aluminum- MD simulations of ramp compression



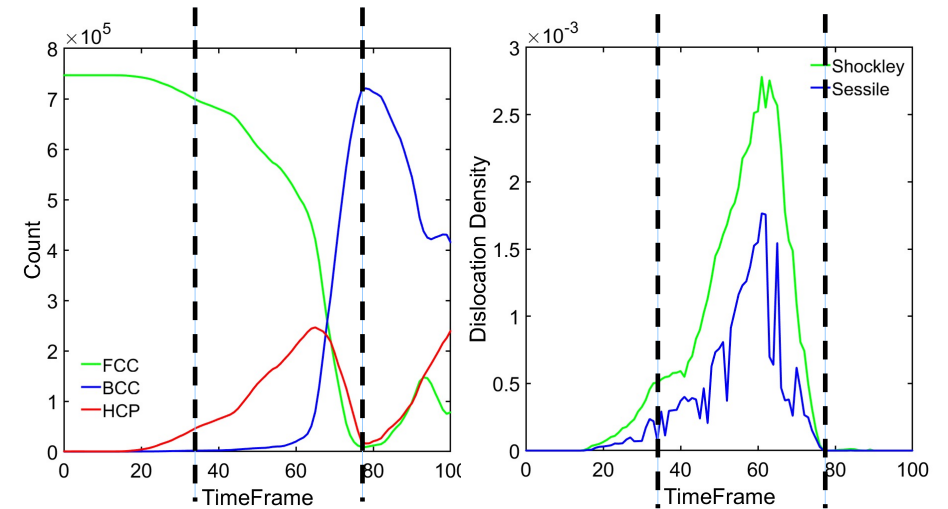
Left boundary is the ramp, which accelerate from 0 – 6 km/s.

Right boundary is a momentum mirror, which reflect when they attempt to move through the wall.

- FCC
- HCP
- BCC



Phase transformation nucleation happens at the intersection of two stacking fault planes.
(Dislocation-assisted phase transformation)

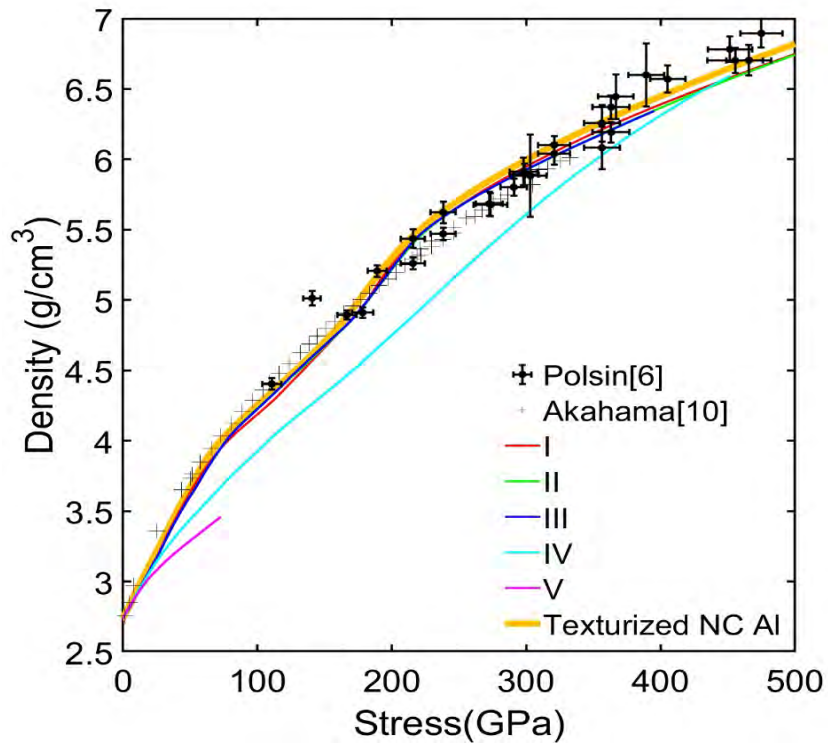


Dislocation density grows significantly at the time when major phase transformation happens



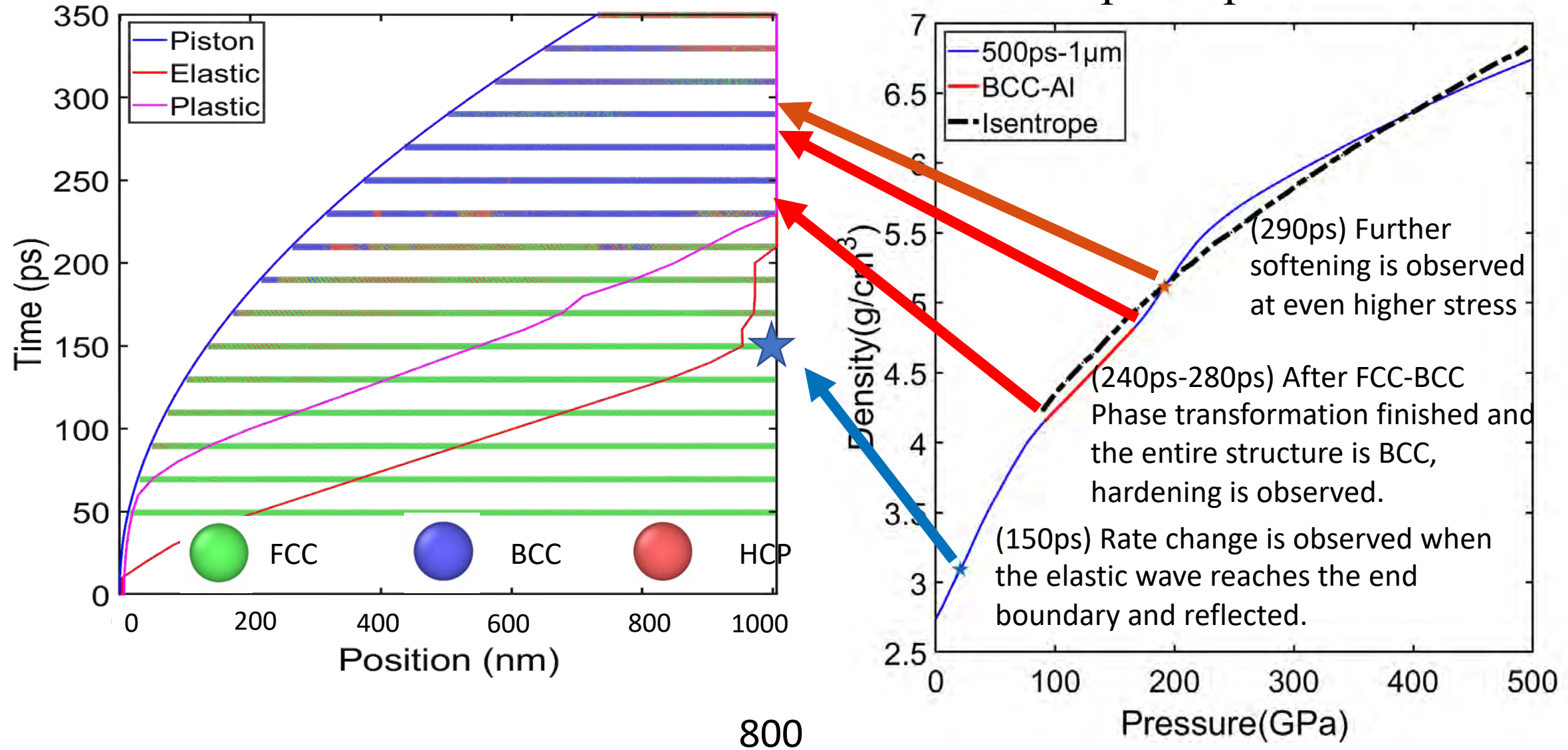
Phase transformation of Aluminum- MD simulations of ramp compression

$$x_s(t_s) = \frac{1}{M} x(t), \quad t_s = \frac{1}{M} t, \quad v_s(t_s) = \frac{\partial x_s}{\partial t_s} = \frac{\frac{1}{M} \partial x}{\frac{1}{M} \partial t} = \frac{\partial x}{\partial t} = v(t) \quad \frac{F_s}{F} = \frac{m_s(L_s/T_s^2)}{m(L/T^2)} = \left(\frac{\rho_s}{\rho}\right) \left(\frac{L_s}{L}\right)^2 \left(\frac{T_s}{T}\right)^{-2} = 1 \quad \dot{v}_p = \frac{v_t L}{\tau C_0^2}$$



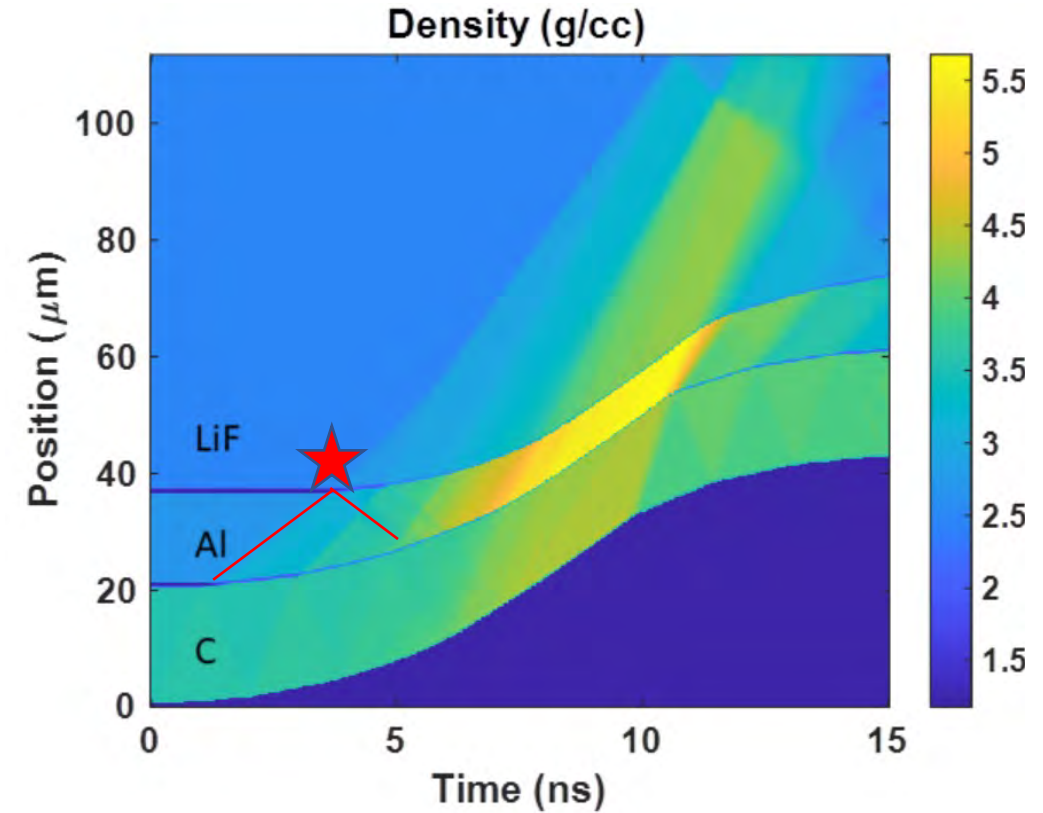
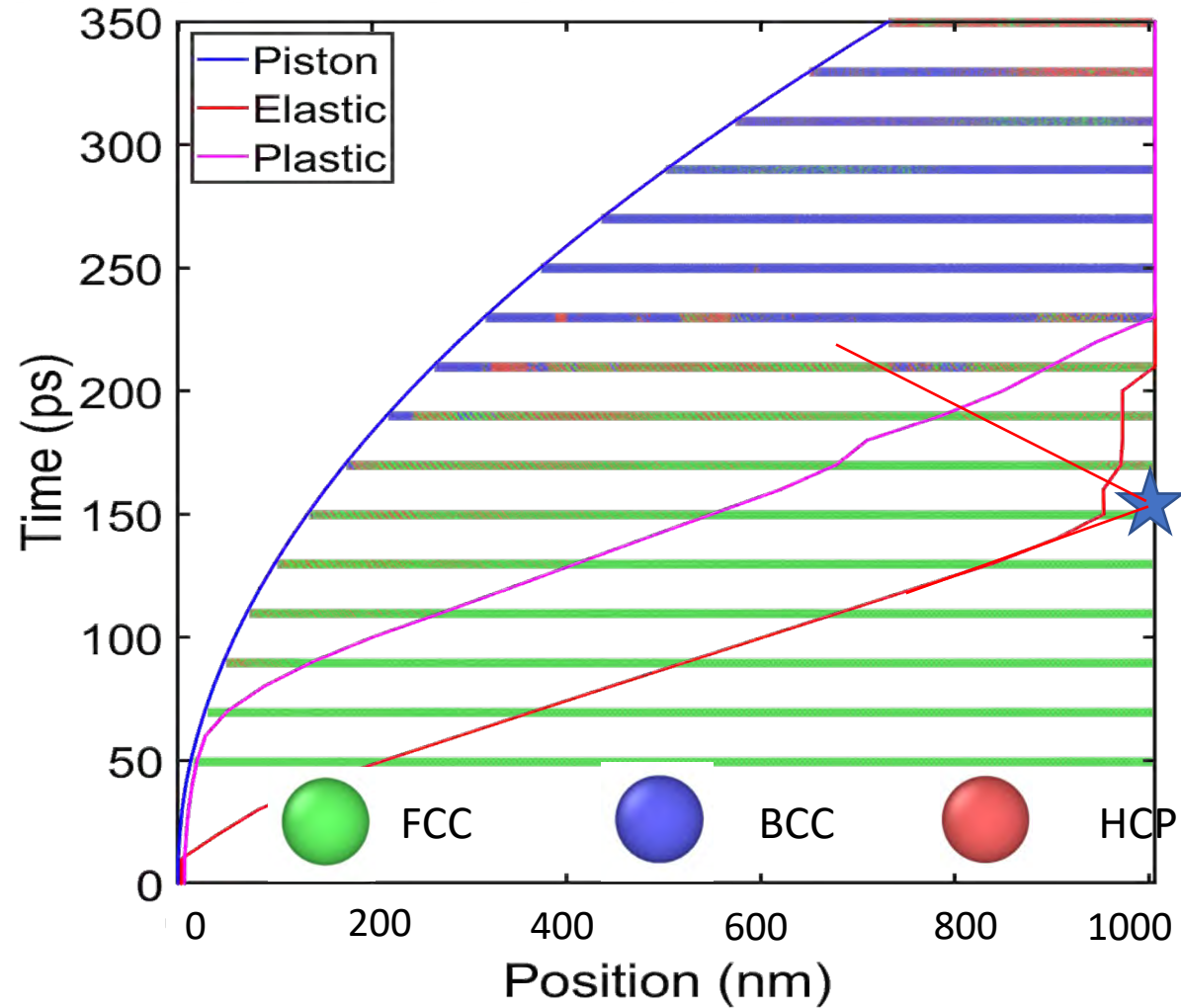
Setup	Length(nm)	Duration(ps)	Length Scale Factor	Time Scale Factor	Atom Count	Dimensionless strain rate
Polsin (Experiment)	20000	10000	1	1	N/A	0.306
I	100	50	1/200	1/200	6.25×10^5	0.306
II	1000	500	1/20	1/20	6.25×10^6	0.306
III	2000	1000	1/10	1/10	1.25×10^7	0.306
IV	1000	250	1/20	1/40	6.25×10^6	0.612
V	2000	250	1/10	1/40	1.25×10^7	1.224
Texturized NC	100	50	1/200	1/200	5.63×10^6 *	0.306

Phase transformation of Aluminum- MD simulations of ramp compression



800

Phase transformation of Aluminum- MD simulations of ramp compression



800

Elastic deformation

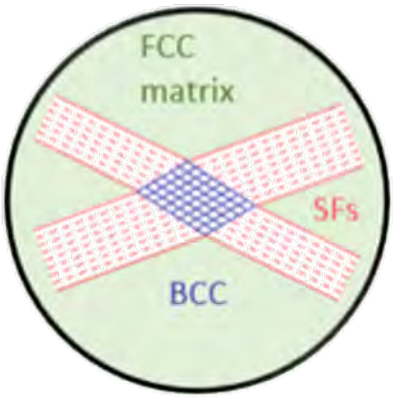
Stacking faults (SFs) formation on (-111) and unzipp (111) micro twins into SFs.

Phase transformation to bcc initiated at the intersecting edges between (-111) and (111) SFs.

Undeformed perfect fcc Al

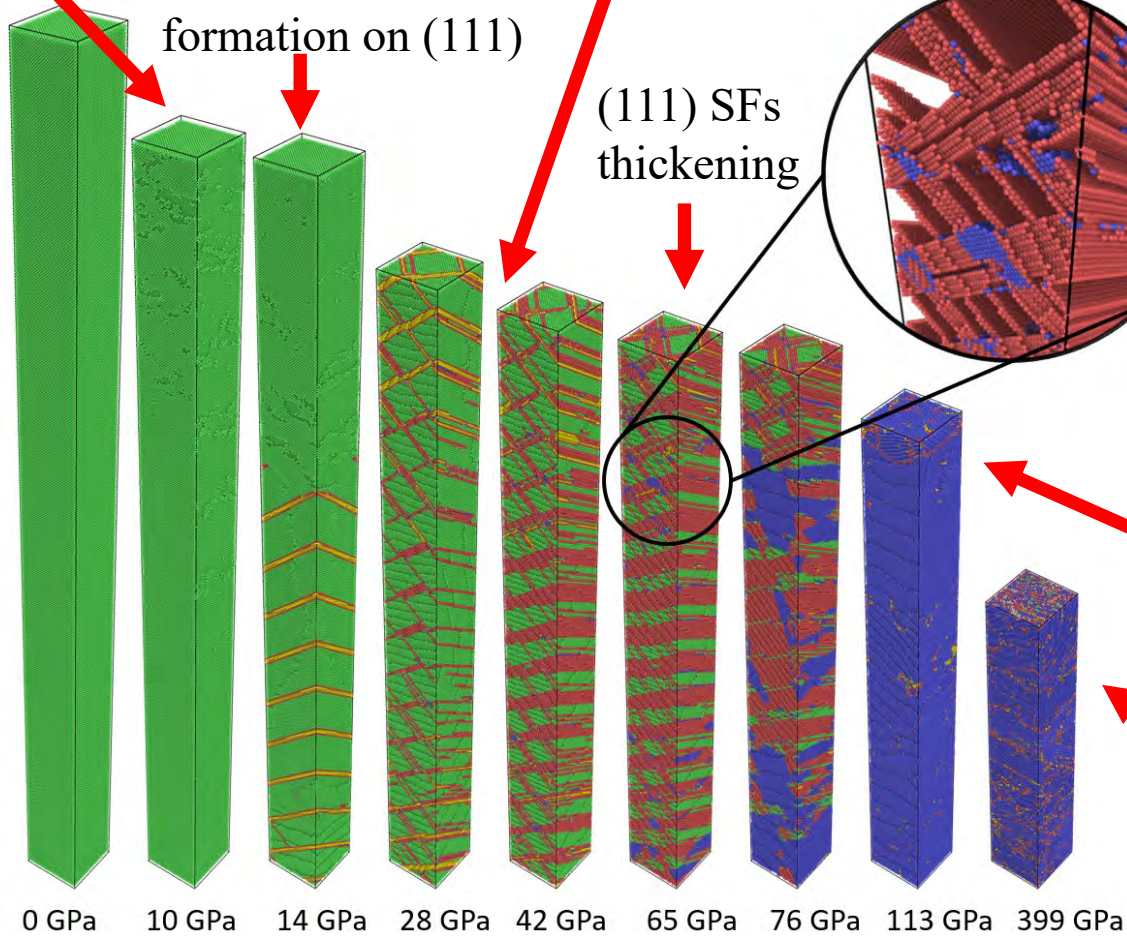
Micro twin formation on (111)

(111) SFs thickening

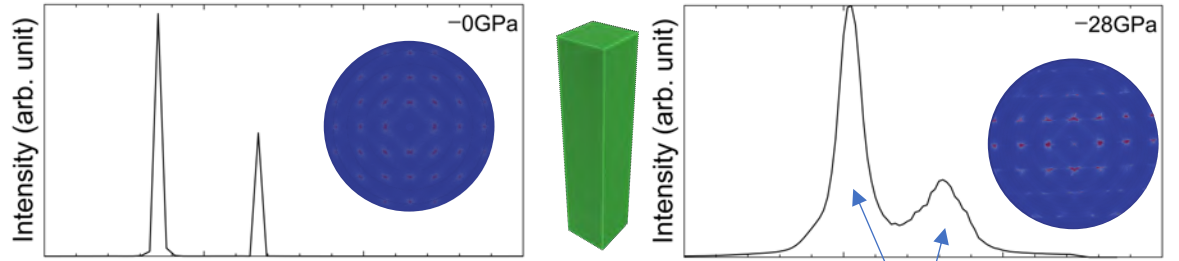


Phase transformation completed, entire structure bcc Al.

Further plasticity in bcc Al.

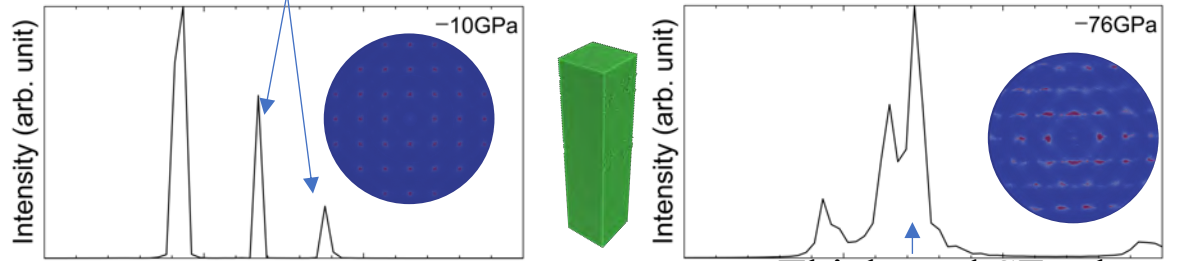


Phase transformation of Aluminum- Virtual XRD and SAED



{200} splitting due to elastic deformation along loading direction

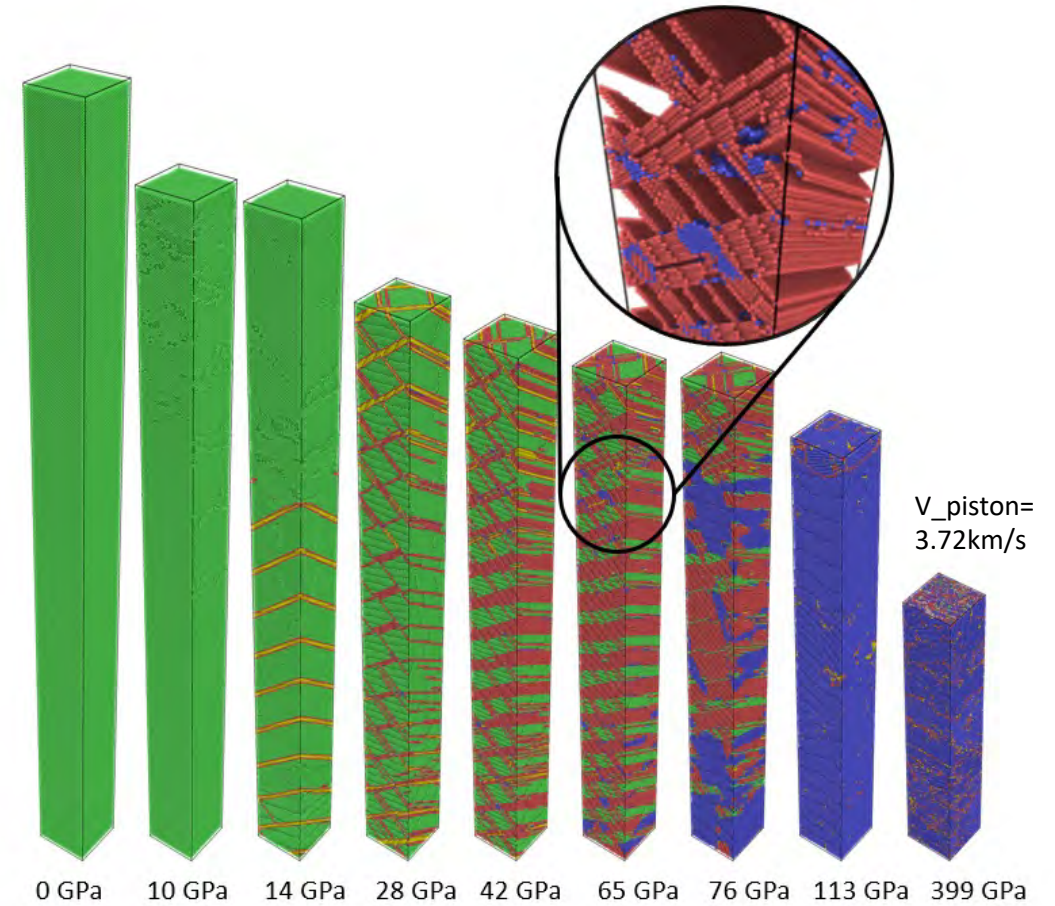
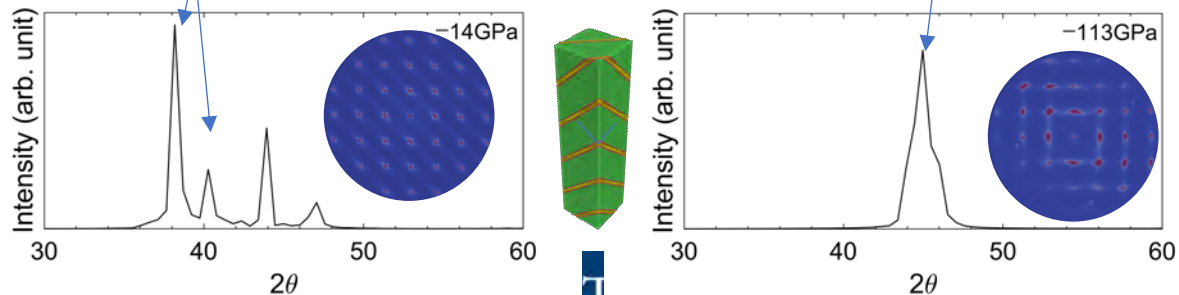
Peaks broadening and relative shifting due to SFs



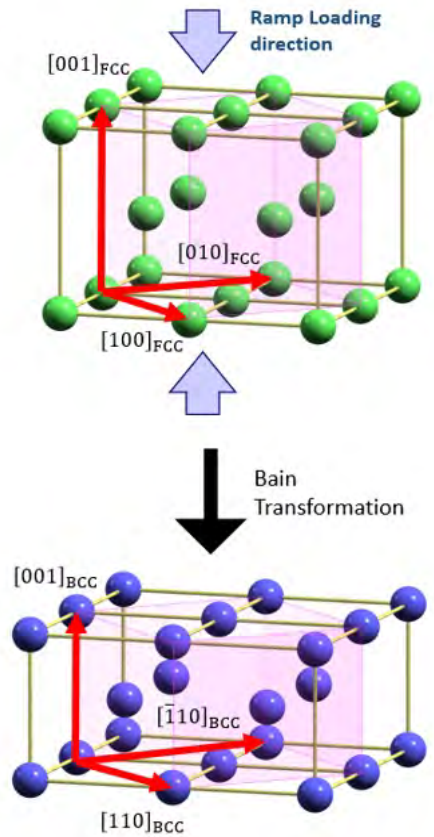
{111} splitting due to inhomogeneous straining caused by micro twin

Thickened SFs show hcp signature

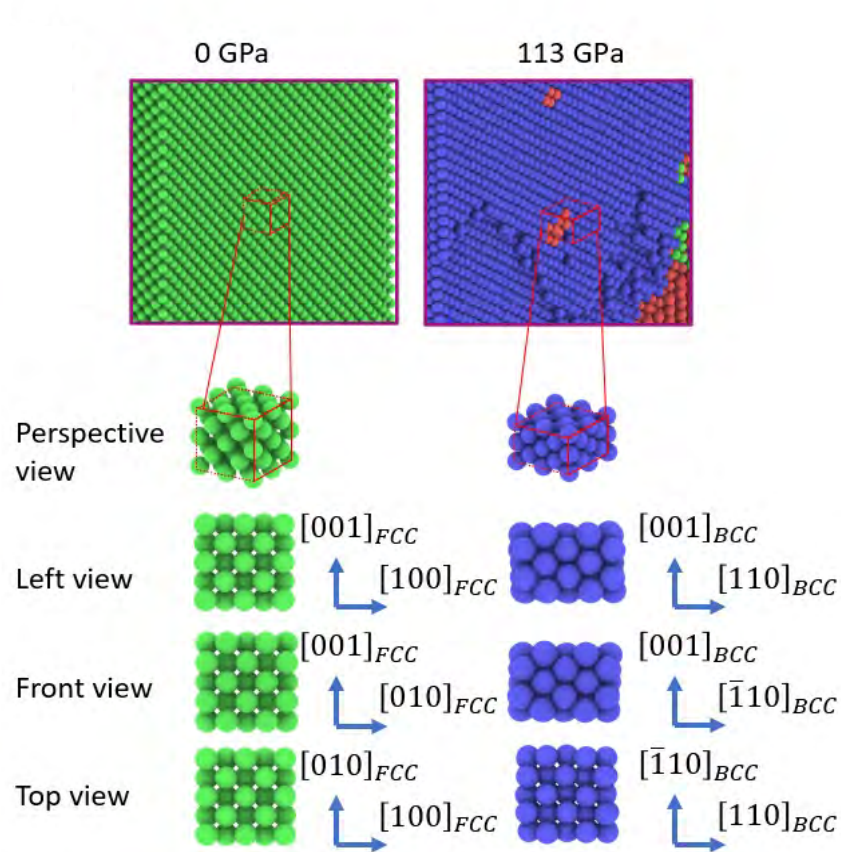
Transformed structure show bcc signature



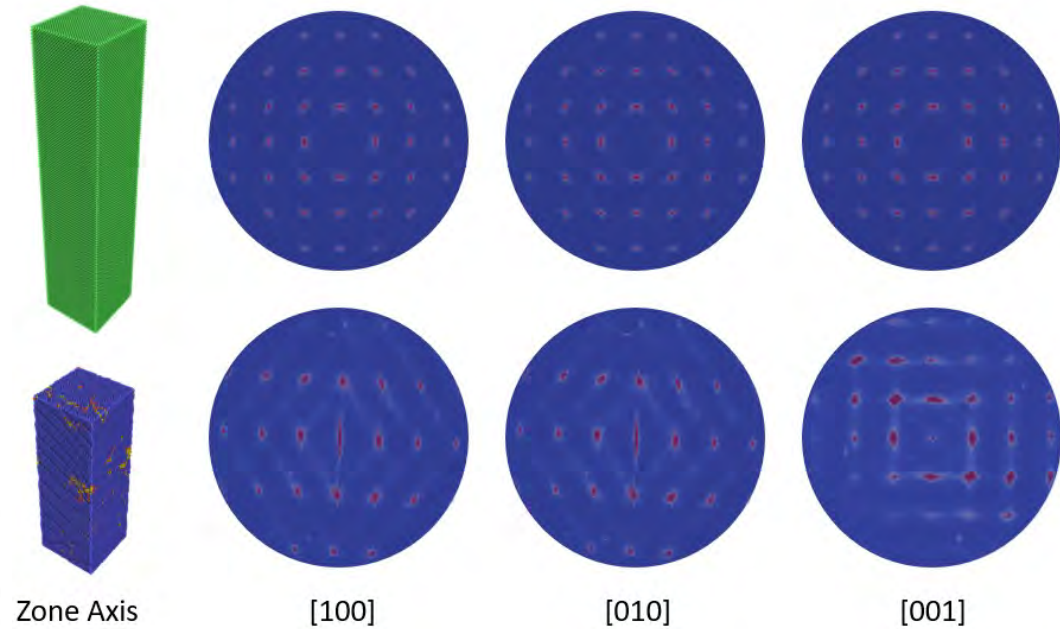
Phase transformation of Aluminum- Bain transformation



Path illustration

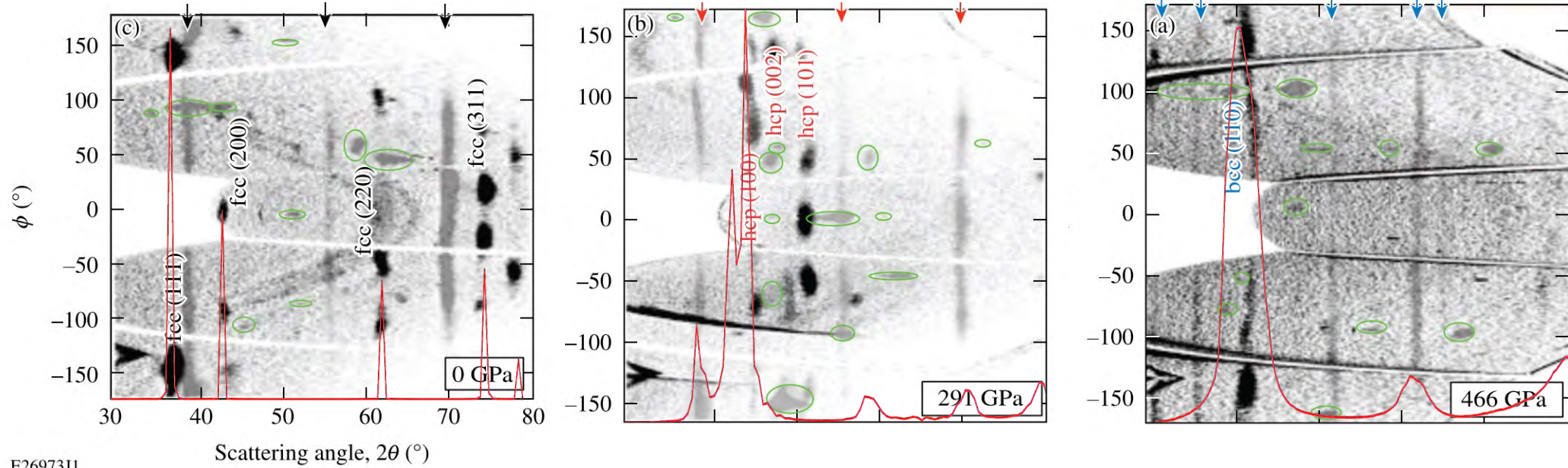


Polyhedral template matching
lattice orientation calculation



Virtual SAED pattern

Phase transformation of Aluminum- comparison with experiments



E26973J1

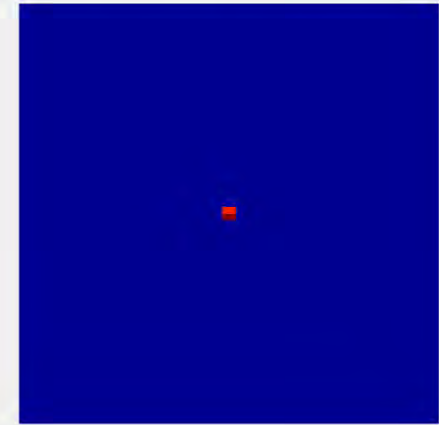
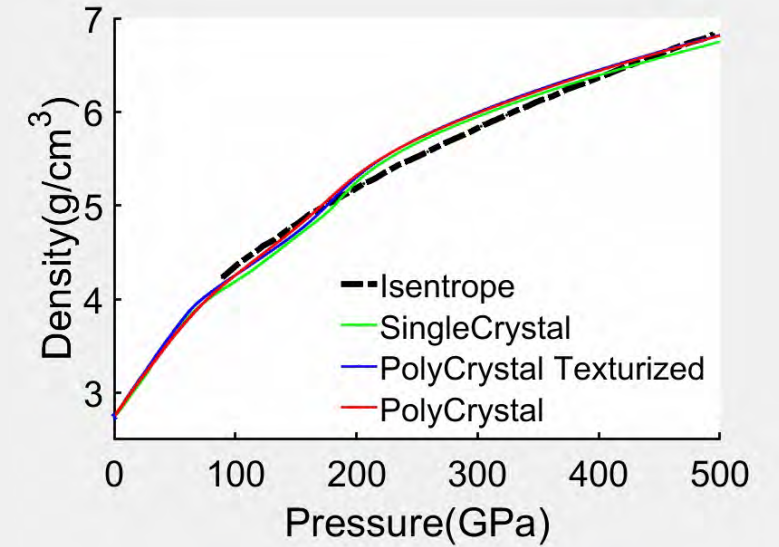
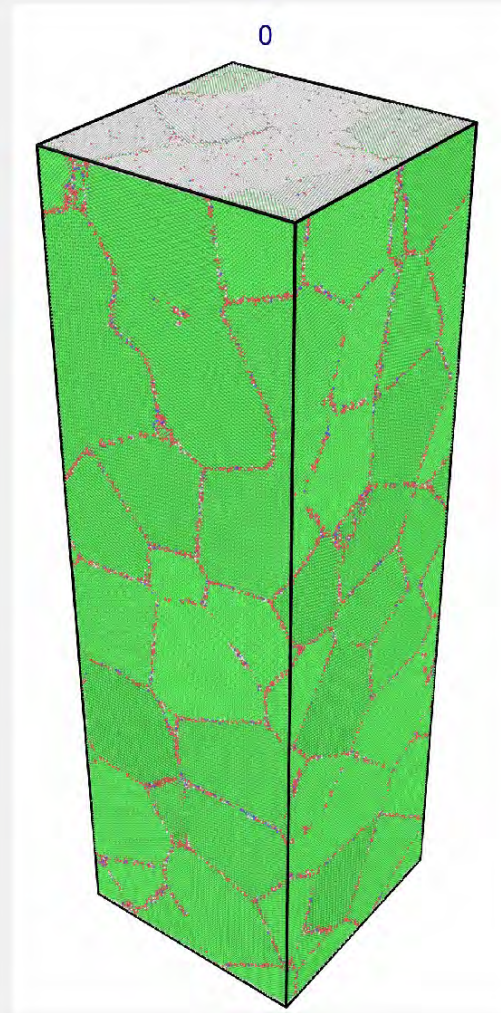
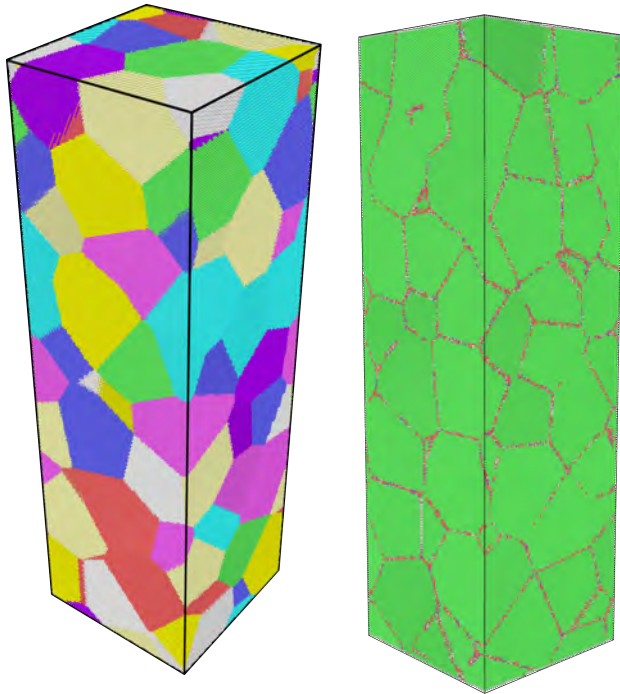
XRD	Stress at which the 1 st figure (fcc) is taken	Stress at which the 2 nd figure (hcp) is taken	Stress at which the 3 rd figure (bcc) is taken
Experiment	0 GPa	291 GPa	466 GPa
Simulation	0 GPa	76 GPa	399 GPa

*Polsin. D. N. et al., Phys. Plasmas 25, 082709 (2018)

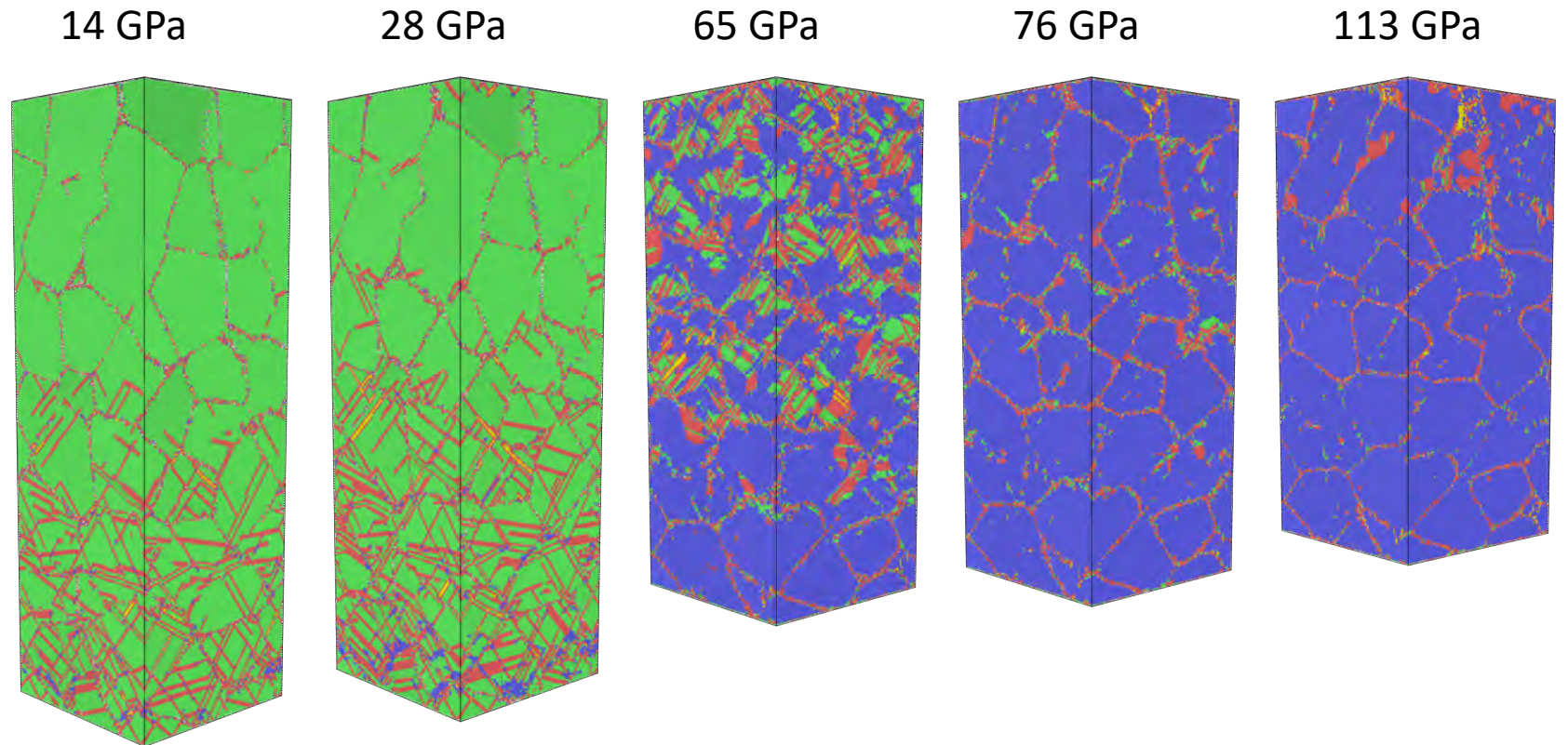
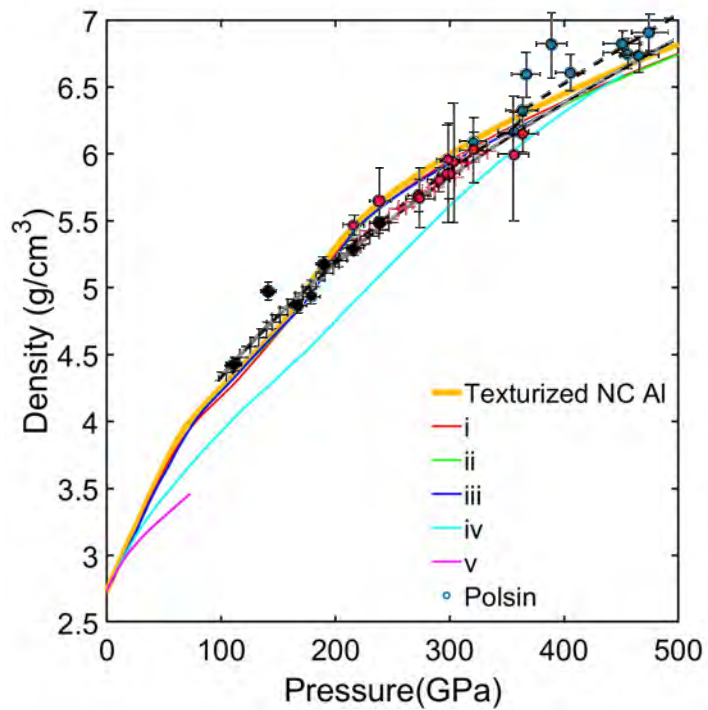


Phase transformation of Aluminum- Texturized nanocrystalline (NC) sample

- Average grain size: 15 nm
- [001]-oriented FCC texturized
- Dimension is 30.37 nm × 30.37 nm × 100 nm, and a scaling factor of 1/200 is used



Phase transformation of Aluminum- Texturized nanocrystalline (NC) sample



Phase transformation of Aluminum- Dislocation assisted Bain Transformation

Experiment observation

- Norm to $(200)_{\text{HCP}}$ have angle of 45-50 degrees to the fiber axis
- Norm to $(110)_{\text{BCC}}$ have angle of ~50 degrees to the fiber axis
- The lattice constant of bcc is reported ~2.43 at 466 GPa

Simulation observation

- For stacking fault, basal plane $(001)_{\text{HCP}} // (111)_{\text{FCC}}$, therefore normal to the $(002)_{\text{HCP}}$ have angle of 54.7 degree to the fiber axis.
- For bcc in the structure, the Bain transformation predicts a 45 degree between the (110) plane and the fiber axis.
- The lattice constant of BCC is 2.33 at 400 GPa.

Phase transformation of Aluminum- Dislocation assisted Bain Transformation

Experiment observation

- Norm to $(200)_{\text{HCP}}$ have angle of 45-50 degrees to the fiber axis
- Norm to $(110)_{\text{BCC}}$ have angle of ~50 degrees to the fiber axis
- The lattice constant of BCC is reported ~2.43 at 466 GPa

Simulation observation

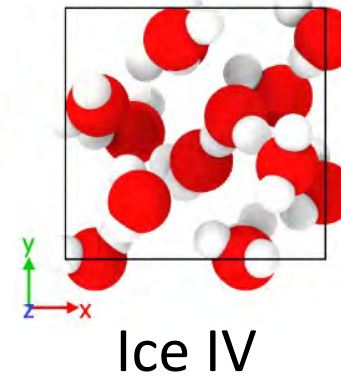
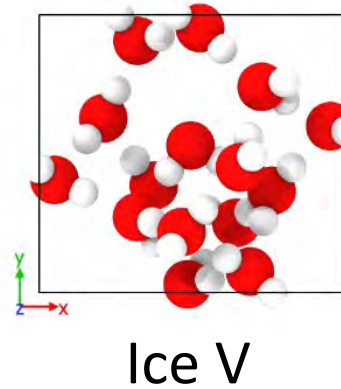
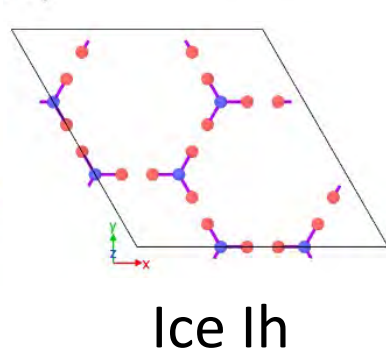
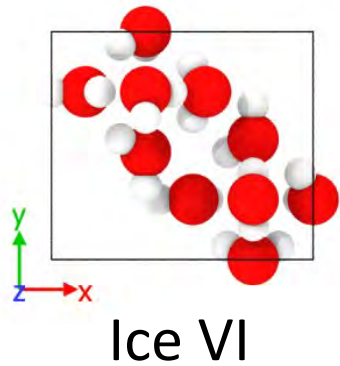
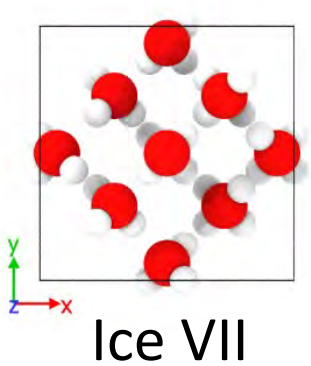
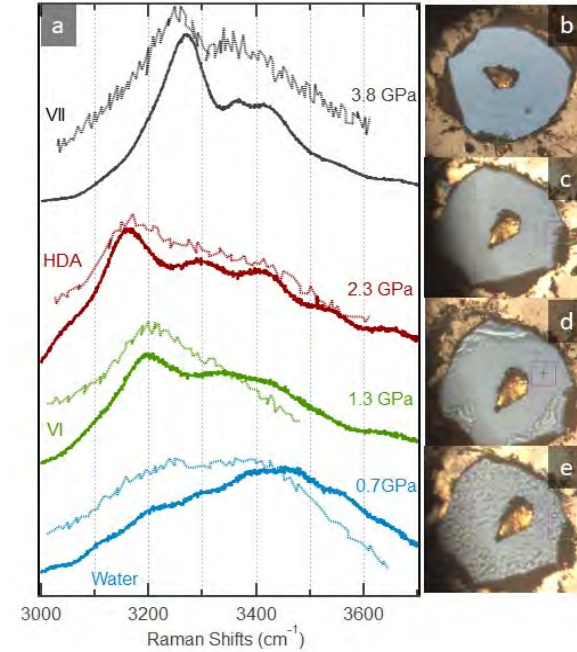
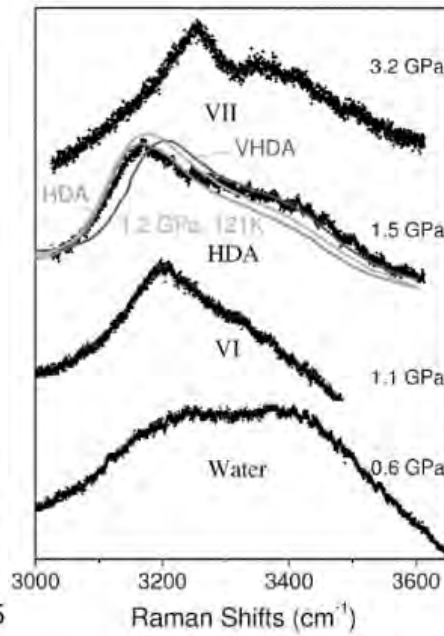
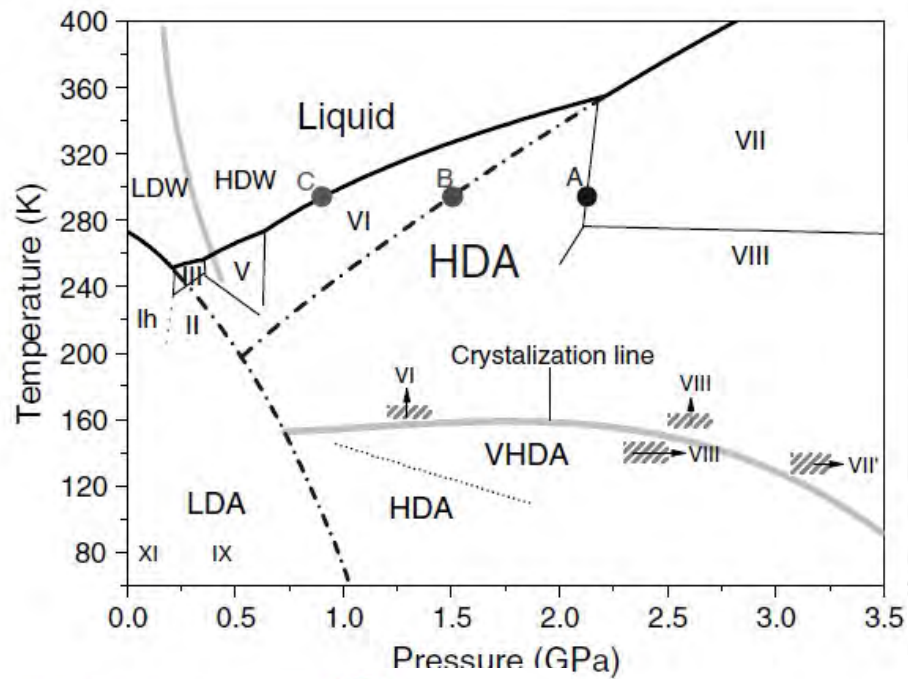
- For stacking fault, basal plane $(001)_{\text{HCP}} // (111)_{\text{FCC}}$, therefore normal to the $(002)_{\text{HCP}}$ have angle of 54.7 degree to the fiber axis.

hydrostatic pressure favors transformations that result in a negative volumetric change and hinders those that result in a positive volumetric change

SEHITOGLU et al., Metallurgical and Materials Transactions, 1996

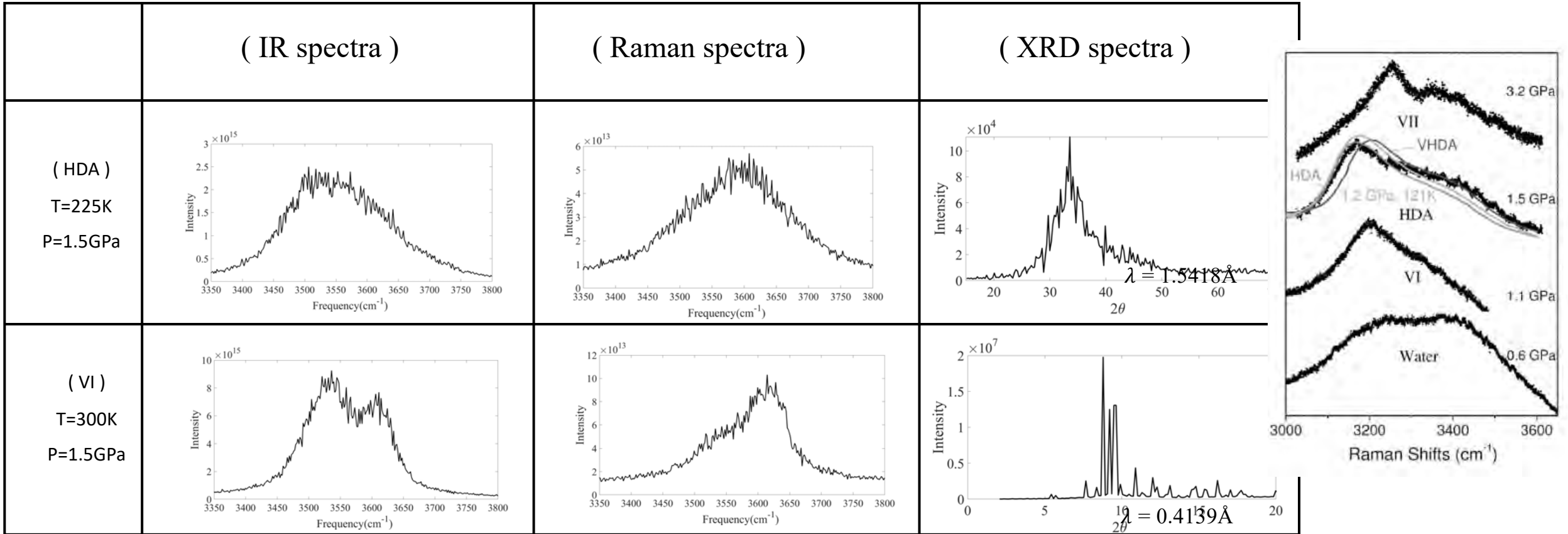


Phase identification of water at ambient temperature



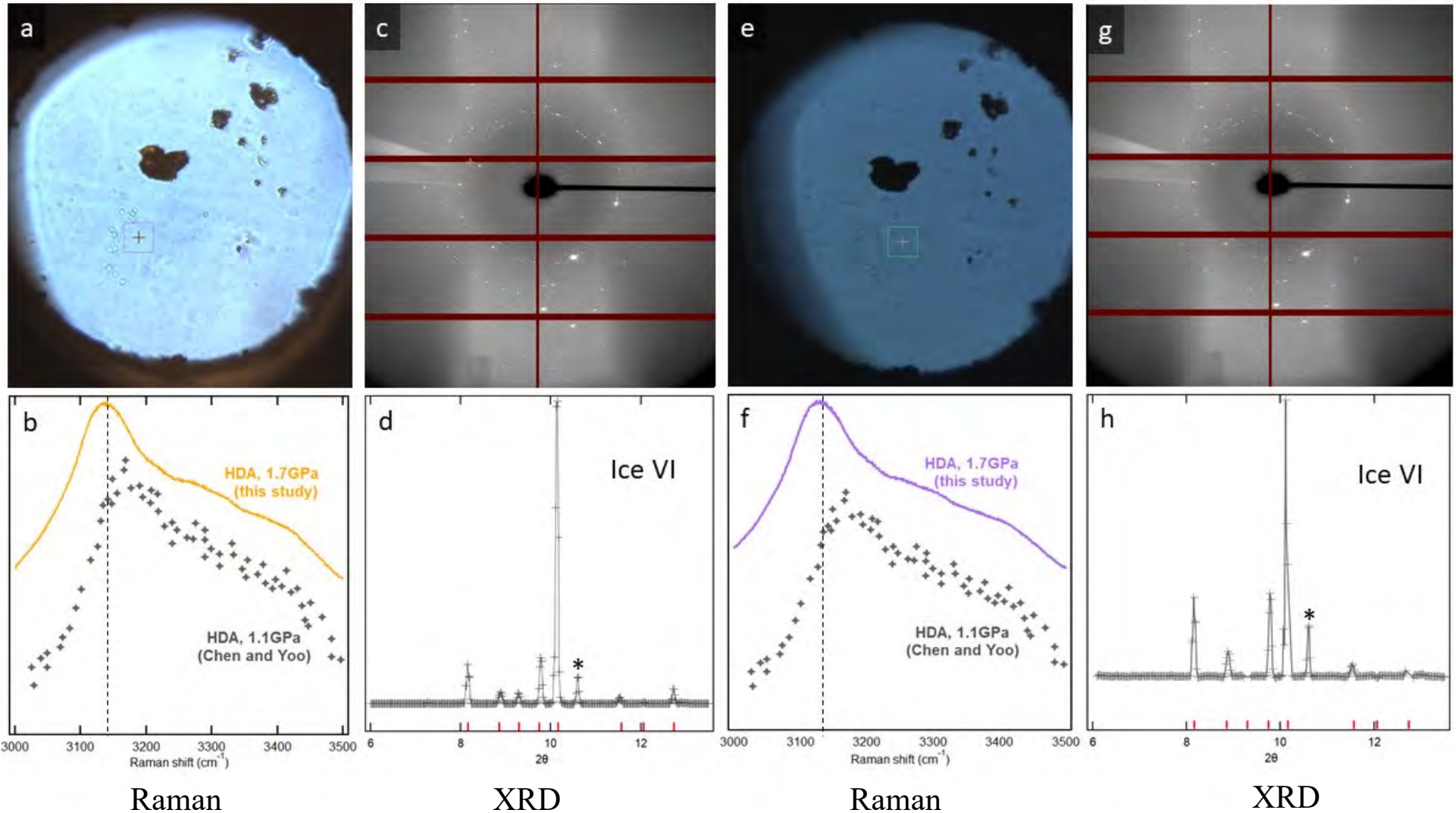
[1] Chen, J. Y., & Yoo, C. S. (2011). High density amorphous ice at room temperature. *Proceedings of the National Academy of Sciences*, 108(19), 7685-7688.

Phase identification of water- Spectra comparison

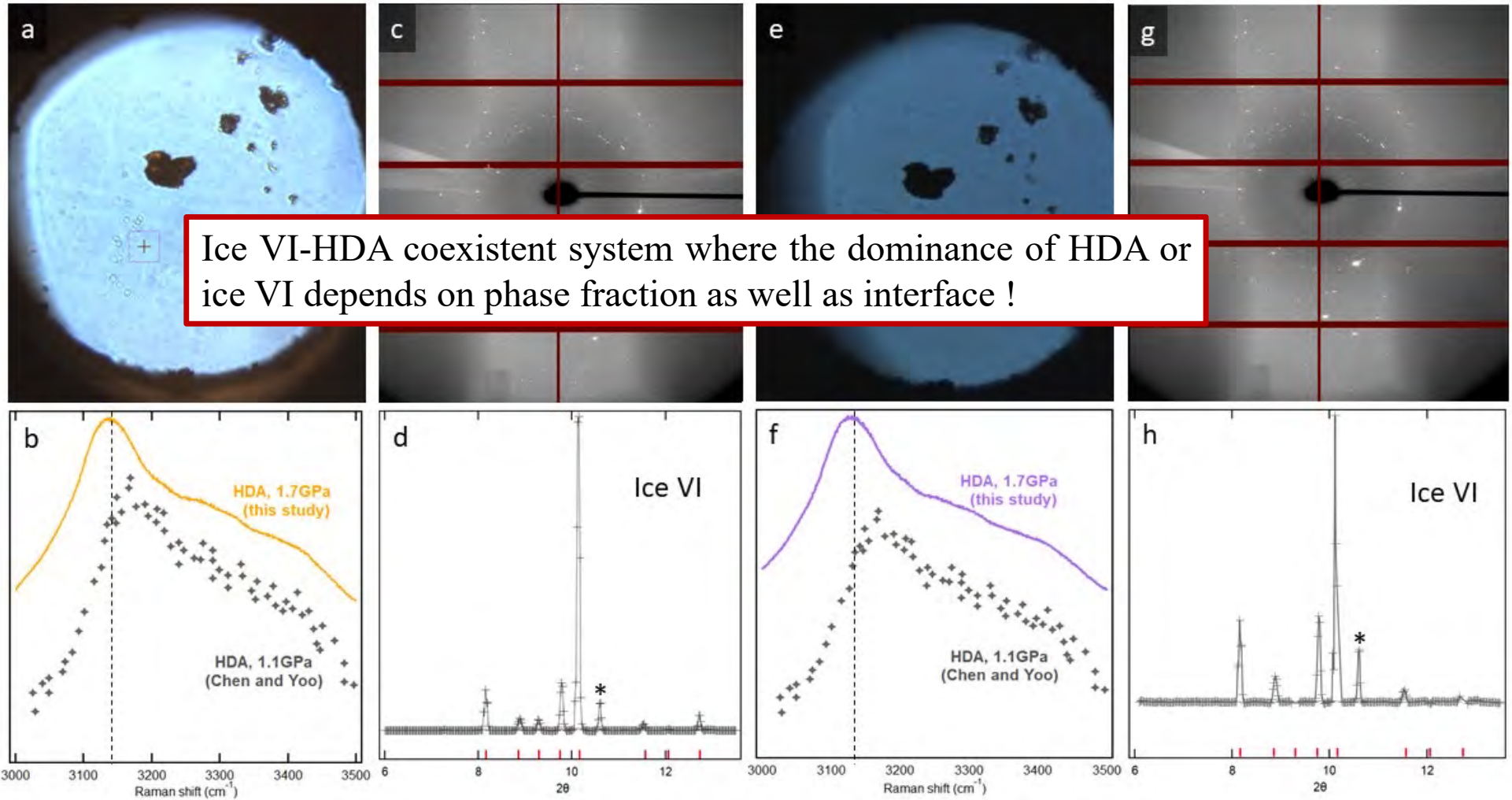


→ [1] Chen, J. Y., & Yoo, C. S. (2011). High density amorphous ice at room temperature. *Proceedings of the National Academy of Sciences*, 108(19), 7685-7688.

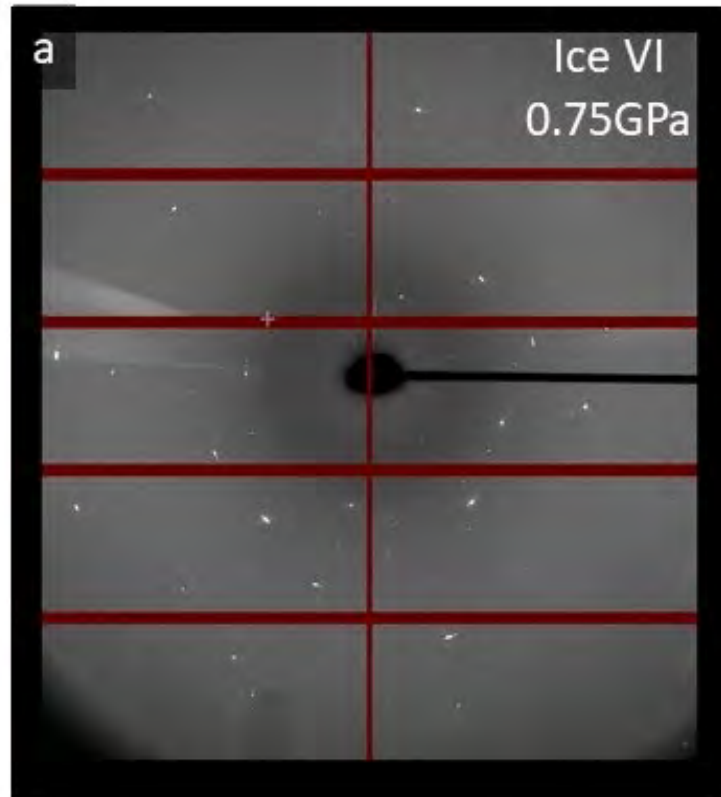
Phase identification of water at ambient temperature



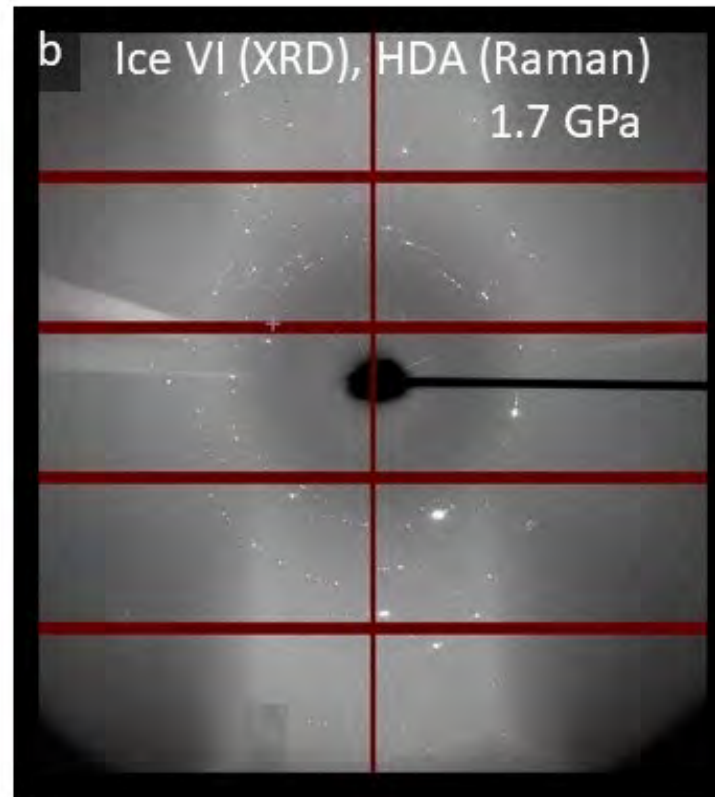
Phase identification of water at ambient temperature



Phase identification of water at ambient temperature



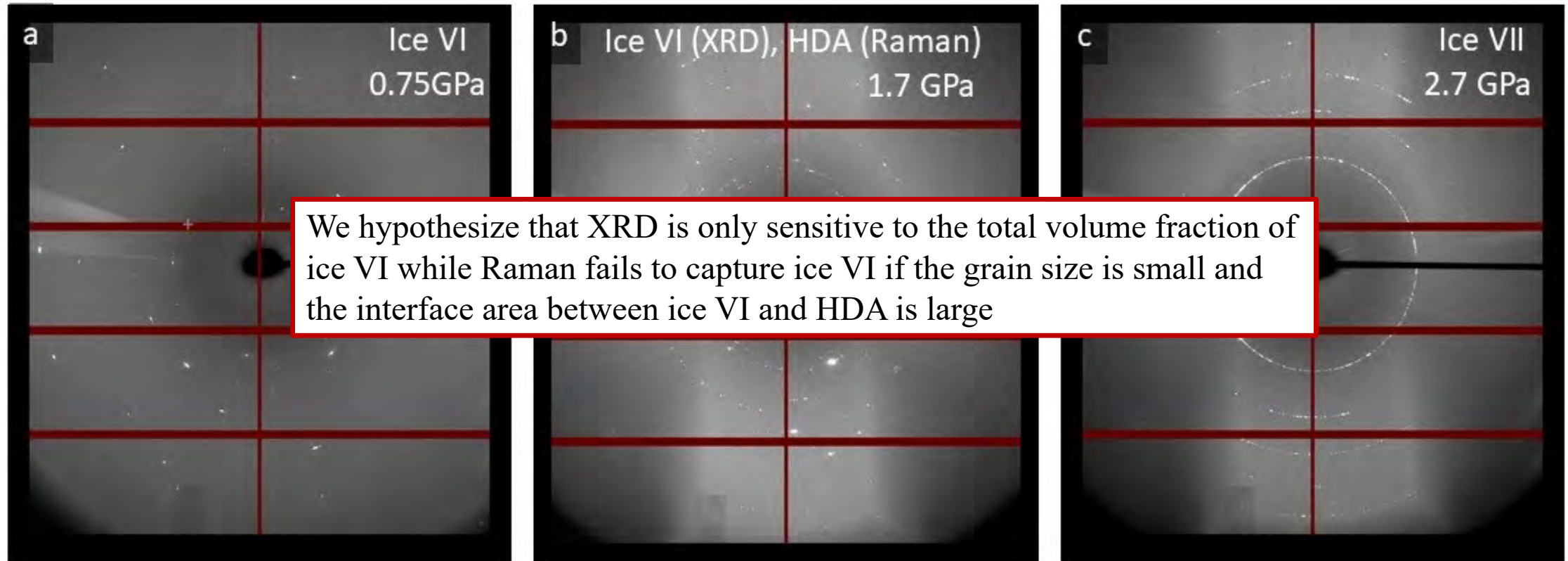
Ice VI grain size $\sim 2\text{-}3\ \mu\text{m}$



Ice VI grain size $\sim 0.5\text{-}1\ \mu\text{m}$



Phase identification of water at ambient temperature



Ice VI grain size $\sim 2-3 \mu\text{m}$

Ice VI grain size $\sim 0.5-1 \mu\text{m}$

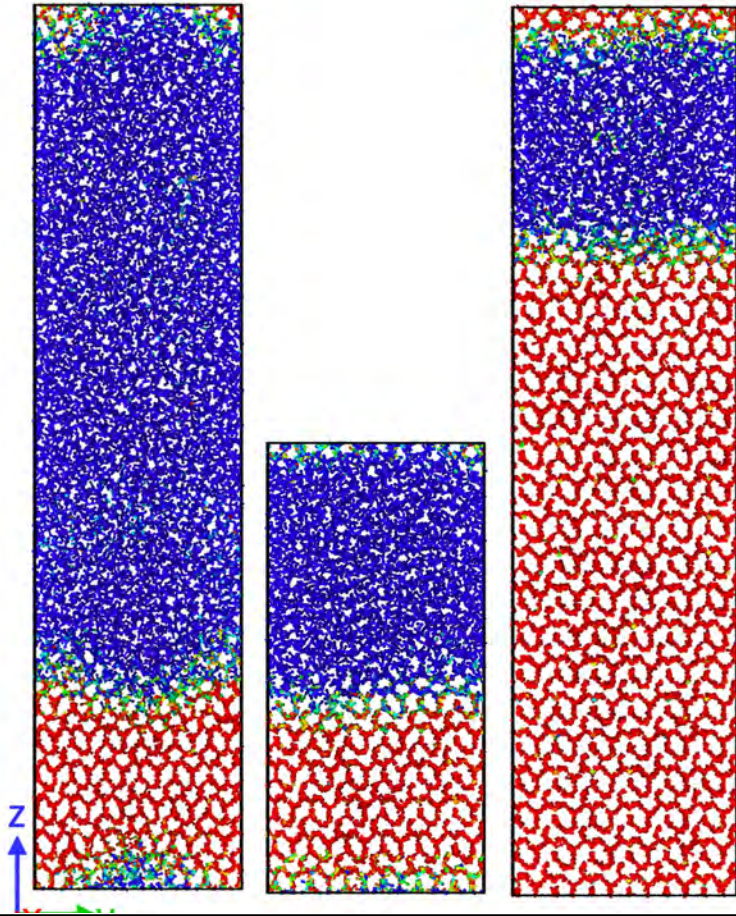
Phase identification of water at ambient temperature

(Effects of phase fraction)

$$\frac{N_{VI}}{N_{HDA}} = \frac{1}{3}$$

$$\frac{N_{VI}}{N_{HDA}} = \frac{1}{1}$$

$$\frac{N_{VI}}{N_{HDA}} = \frac{3}{1}$$

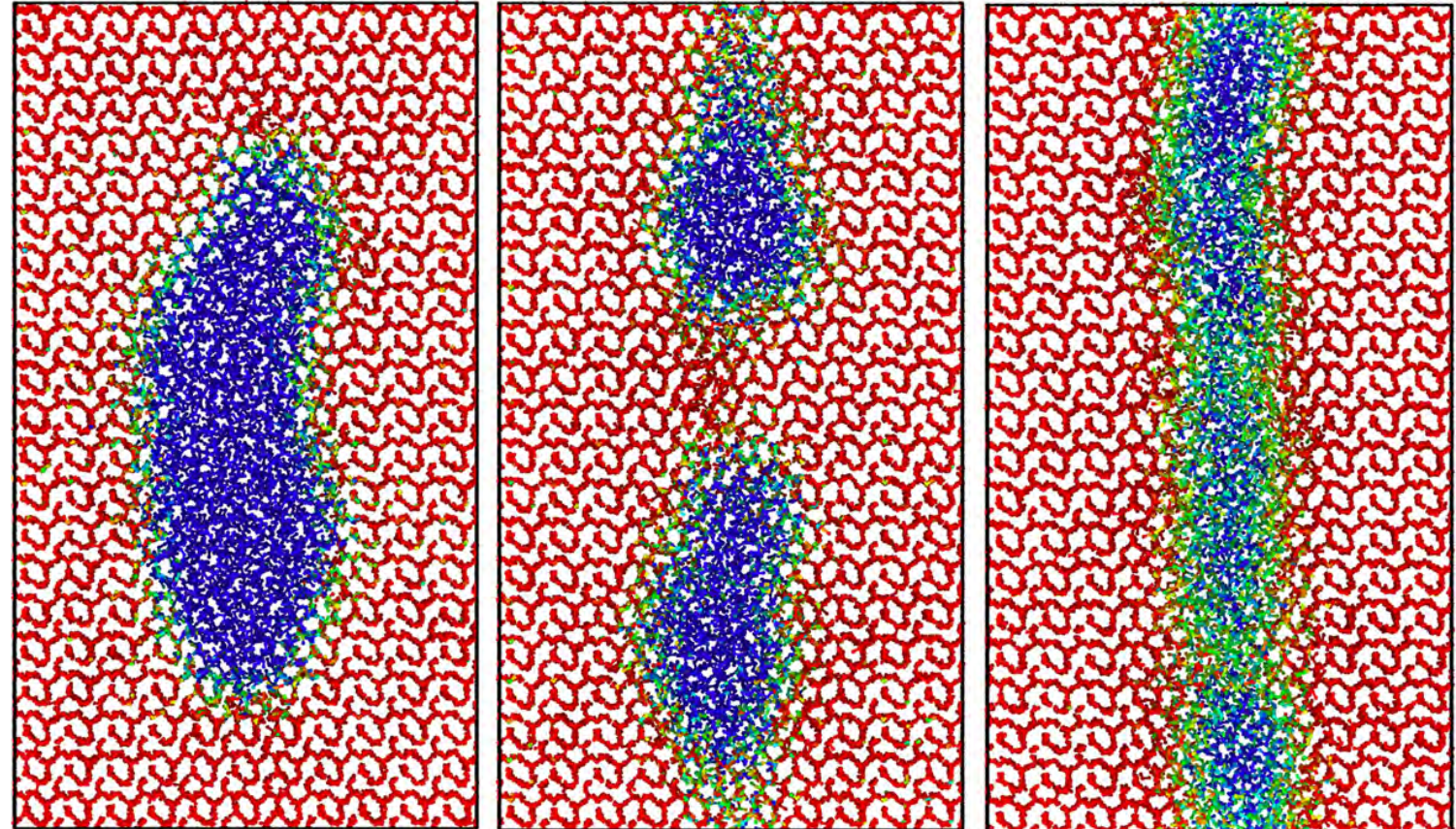


(Effects of interface)

$$\frac{N_{VI}}{N_{HDA}} = 2.27$$

$$\frac{N_{VI}}{N_{HDA}} = 2.24$$

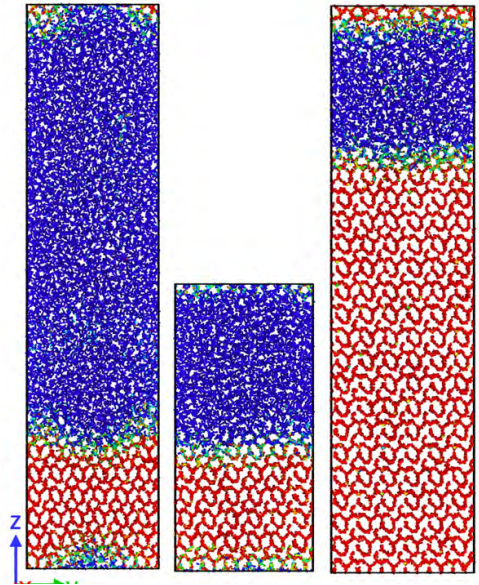
$$\frac{N_{VI}}{N_{HDA}} = 2.18$$



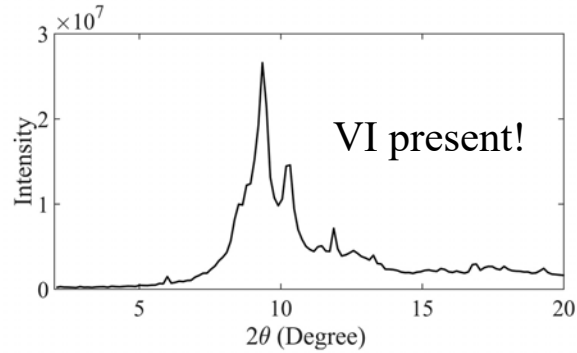
Phase identification of water at ambient temperature

(Effects of phase fraction)

$$\frac{N_{VI}}{N_{HDA}} = \frac{1}{3} \quad \frac{N_{VI}}{N_{HDA}} = \frac{1}{1} \quad \frac{N_{VI}}{N_{HDA}} = \frac{3}{1}$$

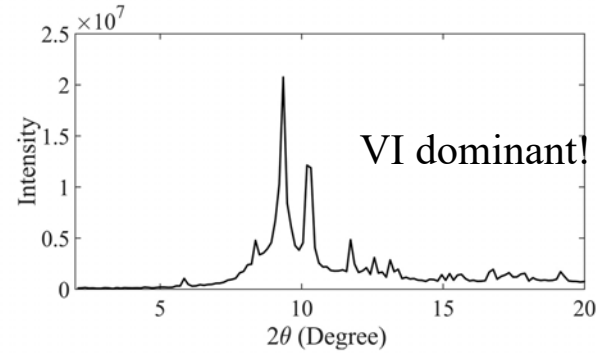


$$\left(\frac{N_{VI}}{N_{HDA}} = \frac{1}{3} \right)$$



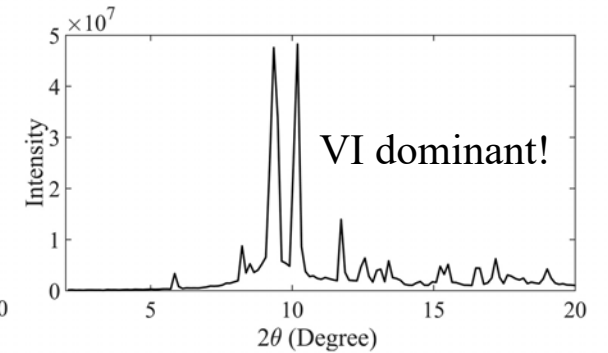
(a)

$$\left(\frac{N_{VI}}{N_{HDA}} = \frac{1}{1} \right)$$

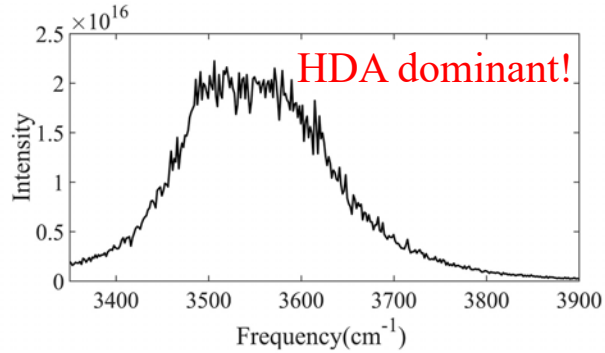


(b)

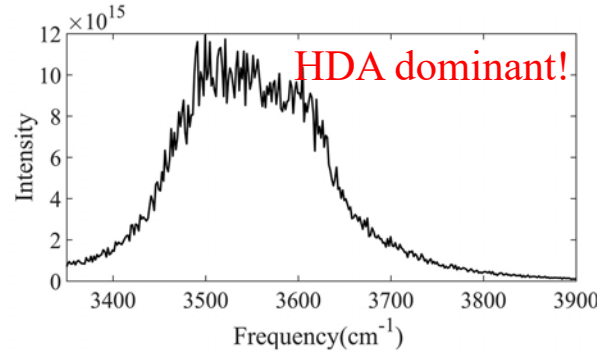
$$\left(\frac{N_{VI}}{N_{HDA}} = \frac{3}{1} \right)$$



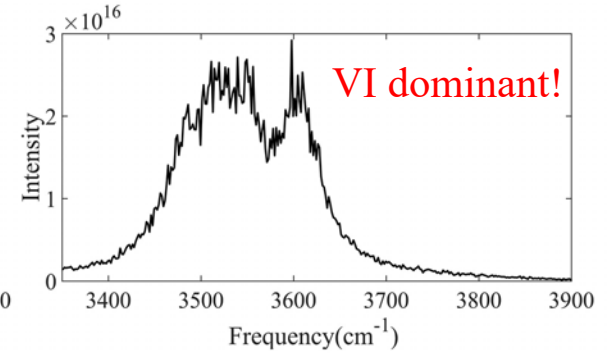
(c)



(d)



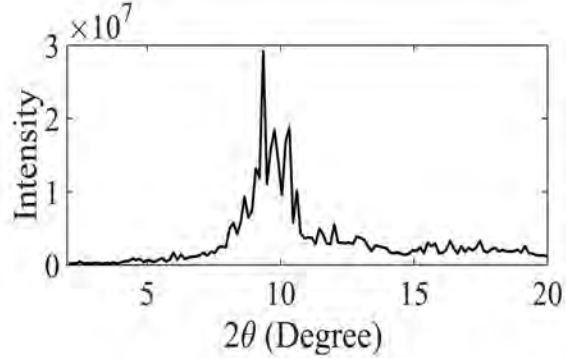
(e)



(f)

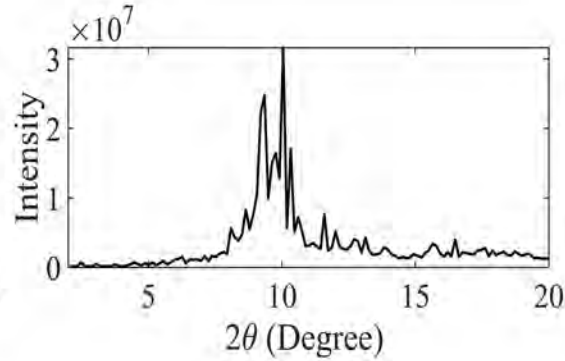
Phase identification of water at ambient temperature

$$\frac{N_{VI}}{N_{HDA}} = 2.27$$



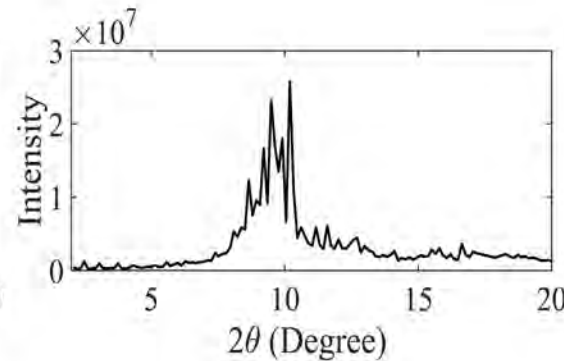
(a)

$$\frac{N_{VI}}{N_{HDA}} = 2.24$$



(b)

$$\frac{N_{VI}}{N_{HDA}} = 2.18$$



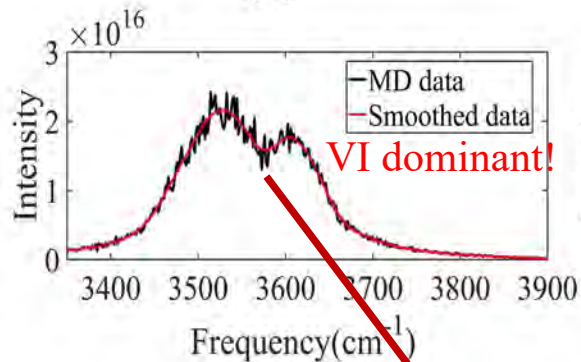
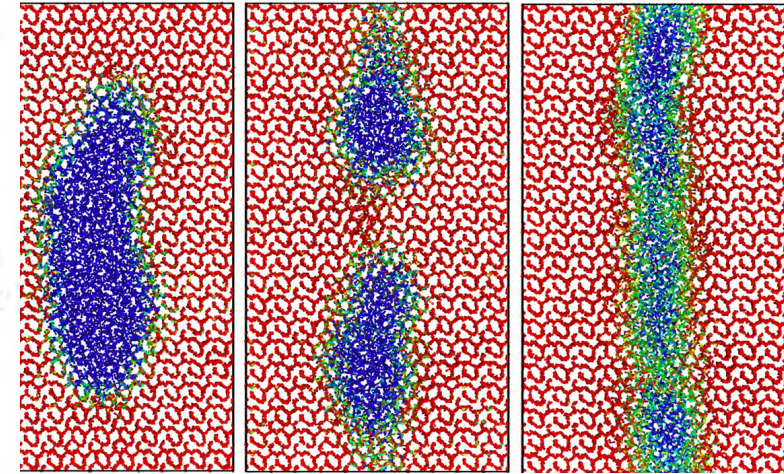
(c)

(Effects of interface)

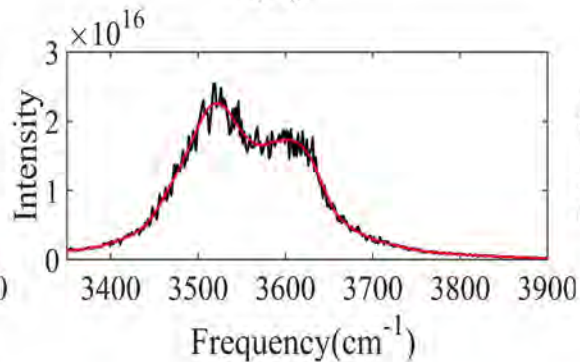
$$\frac{N_{VI}}{N_{HDA}} = 2.27$$

$$\frac{N_{VI}}{N_{HDA}} = 2.24$$

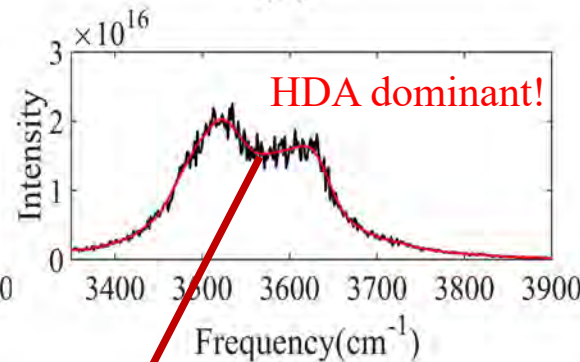
$$\frac{N_{VI}}{N_{HDA}} = 2.18$$



(d)



(e)



(f)

The minima becomes flat by increasing interface area turning into HDA spectra !

coexistent ice VI/HDA system with a large number of small ice VI grains with large interface area with ice HDA regions.

Concluding marks from two studies:

- MD simulations captured the phase transformation mechanisms in Aluminum under high pressures
- Phase transformation and plastic deformation mechanisms are deduced from time-resolved synthetic XRD data
- Good agreement was observed between experimental and synthetic XRD analysis
- Raman and XRD diagnostics presented inconsistent understanding about the the phase of water at high pressure
- MD simulations showed that a water coexistent system explains the uncertainties within experimental Raman and XRD diagnostics



3) Developing AI-powered models for classification of large XRD data

- Time-resolved XRD Images

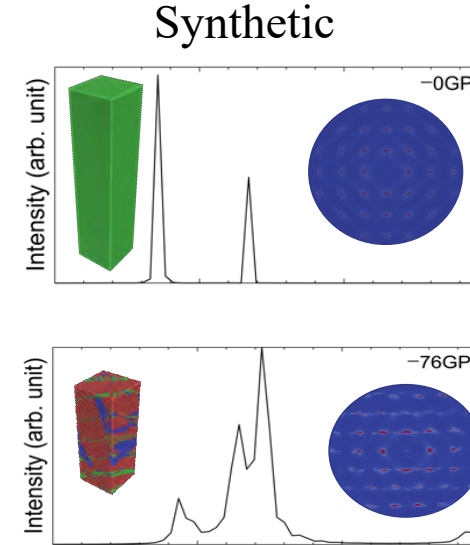
- Data intensive
- Include many uncertainties

- Analyze XRD

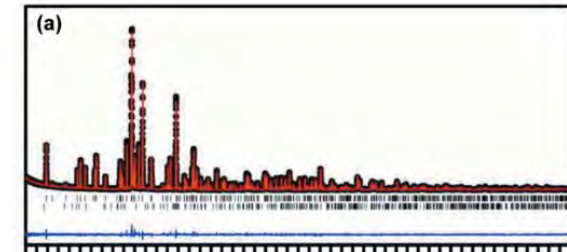
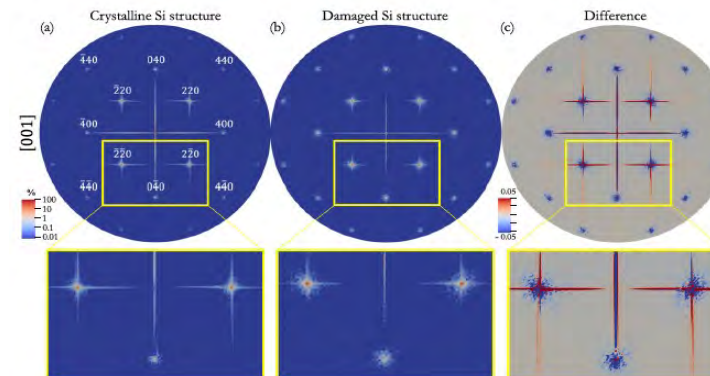
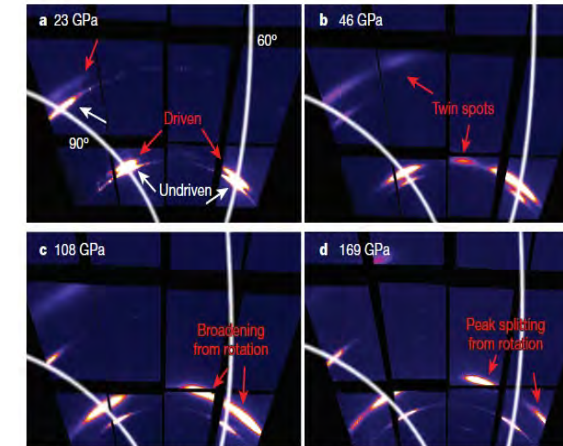
- Human expert
- Conventional indexing software are contentious

- Experimental XRD

- Expensive



Experiments



[2]Coppari, F. et al., 2019. Optimized x-ray sources for x-ray diffraction measurements at the Omega Laser Facility. Review of Scientific Instruments 90, 125113

[3]Park, W.B. et al., 2017. Classification of crystal structure using a convolutional neural network. IUCrJ 4, 486-494.. doi:10.1107/s205225251700714x

3) Developing AI-powered models for classification of large XRD data

- Time-resolved XRD Images

- Data intensive
- Include many uncertainties

- Analyze XRD

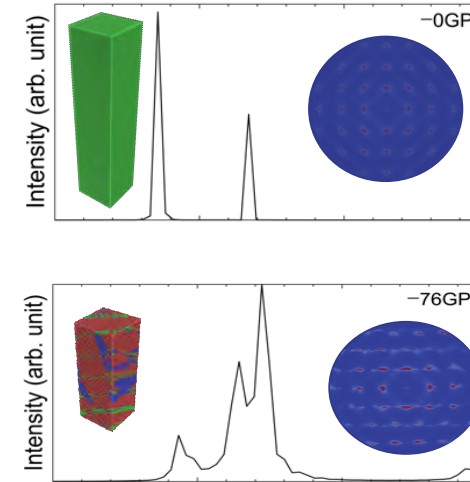
- Human expert
- Conventional indexing software are contentious

Develop automated deep learning computer vision techniques to mine such information-rich data to classify crystal structures and filter and detect lattice-level mechanisms responsible for phase transformation and plastic deformation under extreme conditions

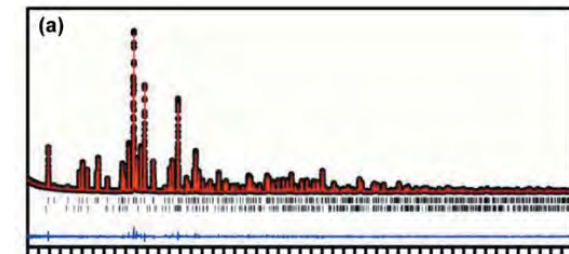
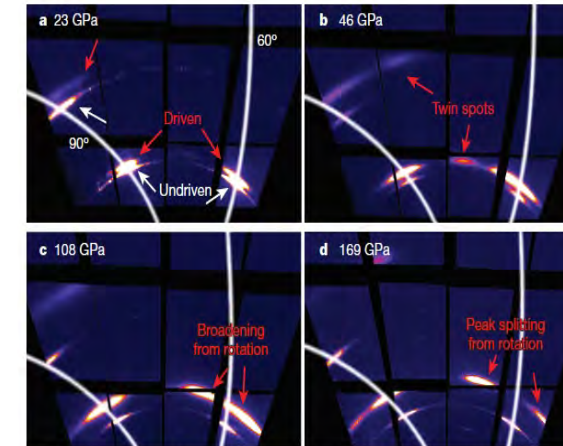
- Experimental XRD

- Expensive

Synthetic



Experiments



[2]Coppari, F. et al., 2019. Optimized x-ray sources for x-ray diffraction measurements at the Omega Laser Facility. Review of Scientific Instruments 90, 125113

[3]Park, W.B. et al., 2017. Classification of crystal structure using a convolutional neural network. IUCrJ 4, 486-494.. doi:10.1107/s205225251700714x



Developing AI-powered models for classification of large XRD data

- Time-resolved XRD Images
 - Data intensive
 - Include many uncertainties
- Generation of static and time-resolved synthetic 1D and 2D XRD images
- Analyze XRD
 - Human expert
 - Conventional indexing software are contentious
- Supervised deep learning for lattice structure classification and temporal lattice dynamics identification
- Interpretation of deep learning models and predictions using explainable deep learning tools
- Experimental XRD
 - Expensive
- Domain adaptation to scarce experimental data

[2]Coppari, F. et al., 2019. Optimized x-ray sources for x-ray diffraction measurements at the Omega Laser Facility. Review of Scientific Instruments 90, 125113

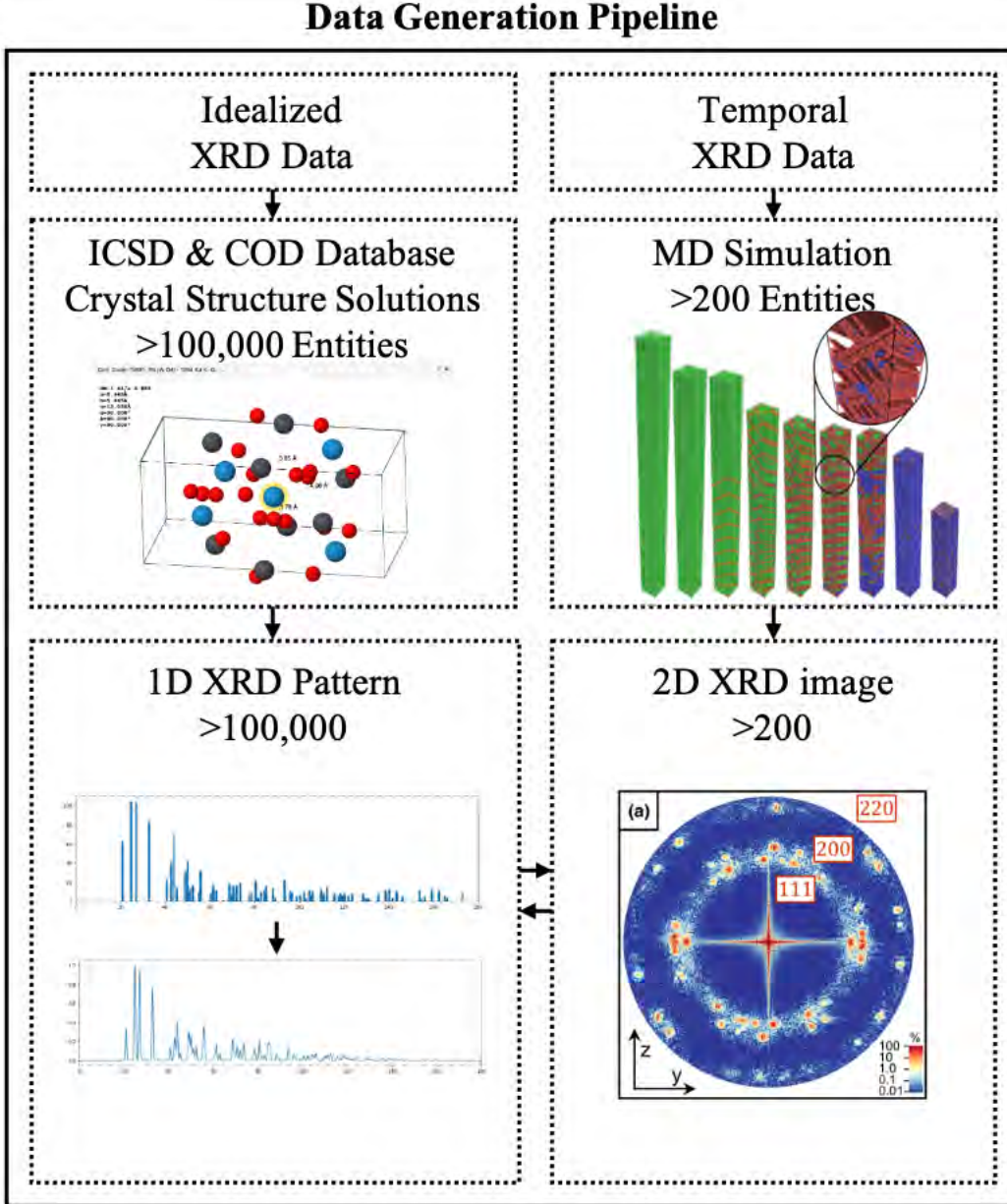
[3]Park, W.B. et al., 2017. Classification of crystal structure using a convolutional neural network. IUCrJ 4, 486-494.. doi:10.1107/s205225251700714x



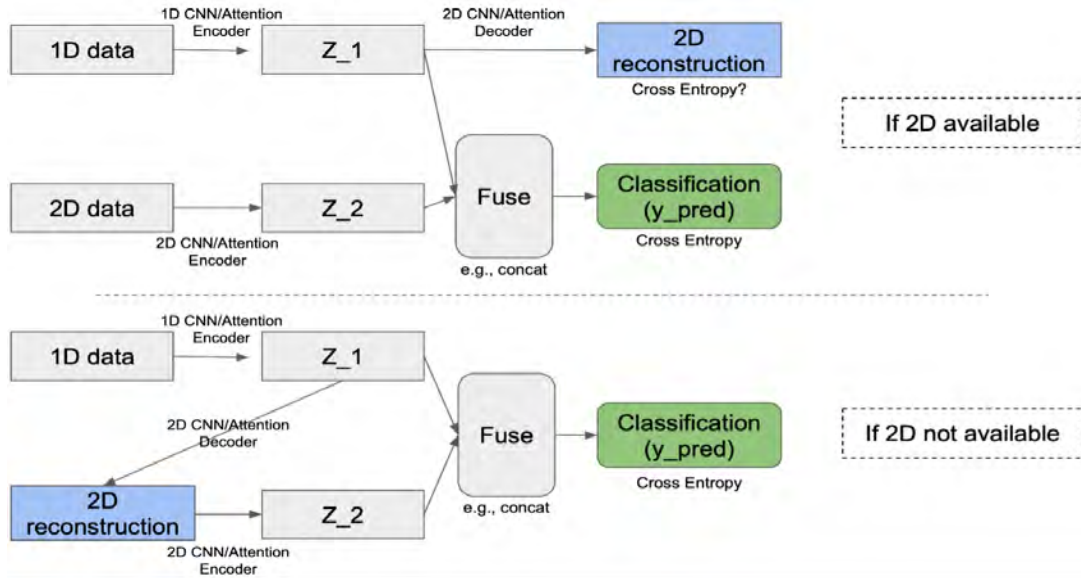
Abbreviation: Classification, Regression, Preprocess, Database, Augmentation, Function, True, False, Experimental, Simulated, ICSD, Cambridge Crystallographic Data Centre,																						
LITERATURE			PREDICTION GOAL			EXPERIMENTAL DATASET				SIMULATED DATASET				MODEL		TRAINING SET	TESTING SET	ACCURACY	MATERIAL			
TITLE	YEAR	TYPE	TYPE	INDEX	NUM	ORIGIN	PRE	AUG	NUM	DB	ORIGIN	PRE	AUG	NUM	TYPE	FUNC						
A data-driven XRD analysis protocol for phase identification...	2021	XRD	C	Phase	21	36, from 3 binary oxides	T	F	36	ICSD	218	T	T	89,943 13,930,000	CNN		80% sim.	20% sim.	94.36	Li-La-Zr-O quaternary compositional		
			R	Phase Fraction	R													exp.	88.88			
																		20% sim. exp.	0.004612 0.008260			
A deep-learning technique for phase identification...	2020	XRD	C	Phase	38	50+50	F	F	50+50	ICSD	170	T	F	800,942	CNN	ReLu	600,942+100,000 sim.	100,000 sim.	100	Sr-Li-Al-O quaternary compositional		
																						50 exp. Li2O...
					Three step phase fraction				3										50		50 exp. SrAl2O4...	98.67
																		100,000 sim.	98			
Crystal symmetry determination...	2020	EBSD	C	Bravais lattices	14	?				?				CNN	ResNet50 Xception	?	50000	93.5	Mo3Si, Al, Ta, Ti, Ilmenite, Sn, Anatase, +7...			
														CNN	ResNet50 Xception			>90				
																		300000		>90		
Rapid Identification of X-ray Diffraction Patterns Based on Very Limited...	2020	XRD	C	material one-by-one	1012	10	T	T	10*3=30	CCD C	1012	T	T	1012*72=72864	CNN	ReLu Adam Keras TensorFlow	58,292 (80% sim.)	14,572 (20% sim.)	Unknown	1012 patterns sim.		
																				30 exp.	96.7	10 MOFs exp.
Fast and interpretable classification...	2019	XRD	C	Dimensionality	3	75/115 88/115	F	T	2000	ICSD	164	T	T	2000	a-CNN		all sim.+80% exp.	20% exp.	92.9	Perovskites-inspired 3D, 2D, 0D		
				Space group	7				2000					2000					89.3			
Insightful classification of crystal structures using deep learning	2018	Diffraction Fingerprints	C	Crystal Structure	8	None				AFL OW LIB	10,517	T	F	10,517	CNN	Adam TensorFlow Keras	90% sim.	10% sim.	100	83 chemical species + manually mapped atomic num.		
																						10,517*10 defected
Classification of crystal structure...	2017	XRD	C	Crystal system	7	1+1	F	F	2	ICSD	150,000	T	F	150,000	CNN	ReLu	80% sim.	20% sim.	94.99	All ICSD database		
																			1+1 exp.		100	
					Extinction Group													101	20% sim.		83.83	
					Space Group													230	1+1 exp.		0	
Generalized machine learning technique for...	2015	XRD Raman Fluore...	C	Phase	4	64	T	T	64	NONE				ML		2/3 exp.	1/3 exp.	99.22	alpha-Al2O3, gamma, theta-Al2O3, NiO, Inconel Oxide			
						144	T	T	144						2/3 exp.	1/3 exp.	97.6					
						144	T	T	144						2/3 exp.	1/3 exp.	95.2					

Abbreviation: Classification, Regression, Preprocess, Database, Augmentation, Function, True, False, Experimental, Simulated, ICSD, Cambridge Crystallographic Data Centre,

LITERATURE		PREDICTION GOAL			EXPERIMENTAL DATASET			SIMULATED DATASET			MODEL		TRAINING SET	TESTING SET	ACCURACY	MATERIAL			
TITLE	YEAR	TYPE	TYPE	INSTRUMENT	CLASSIFICATION	REGRESSION	PREPROCESS	DATABASE	AUGMENTATION	FUNCTION	TRUE	FALSE	EXPERIMENTAL	SIMULATED	ICSD	CAMBRIDGE CRYSTALLOGRAPHIC DATA CENTRE			
A data-driven XRD analysis protocol for phase identification...	2021	XRD	C	Phase									80% sim.	20% sim.	94.36	Li-La-Zr-O quaternary compositional			
			R	Phase										exp.	88.88				
				Phase													20% sim.	0.004612	
A deep-learning technique for phase identification...	2020	XRD	C	Phase									600,942+100,000 sim.	100,000 sim.	100	Sr-Li-Al-O quaternary compositional			
				Phase											50 exp.		100		
				Phase													50 exp.	98.67	
Crystal symmetry determination...	2020	EBSD	C	Bravais lattice									?	50000	93.5	Mo3Si, Al, Ta, Ti, Ilmenite, Sn, Anatase, +7...			
				Bravais lattice													300000	>90	
				Bravais lattice														>90	
Rapid Identification of X-ray Diffraction Patterns Based on Very Limited...	2020	XRD	C	mainone-									58,292 (80% sim.)	14,572 (20% sim.)	Unknown	1012 patterns sim.			
Fast and interpretable classification...	2019	XRD	C	Dimension									all sim.+80% exp.	30 exp.	96.7	10 MOFs exp.			
				Space													20% exp.	92.9	
Insightful classification of crystal structures using deep learning	2018	Diffraction Fingerprints	C	Crystal Structure									90% sim.	10% sim.	100	83 chemical species + manually mapped atomic num.			
				Crystal Structure														10,517*10 defected	>97
Classification of crystal structure...	2017	XRD	C	Crystal System									80% sim.	20% sim.	94.99	All ICSD database			
				Crystal System														1+1 exp.	100
				Crystal System														20% sim.	83.83
				Crystal System														1+1 exp.	0
Generalized machine learning technique for...	2015	XRD Raman Fluorescence	C	Phase									2/3 exp.	1/3 exp.	99.22	alpha-Al2O3, gamma, theta-Al2O3, NiO, Inconel Oxide			
				Phase														1/3 exp.	97.6
				Phase															1/3 exp.

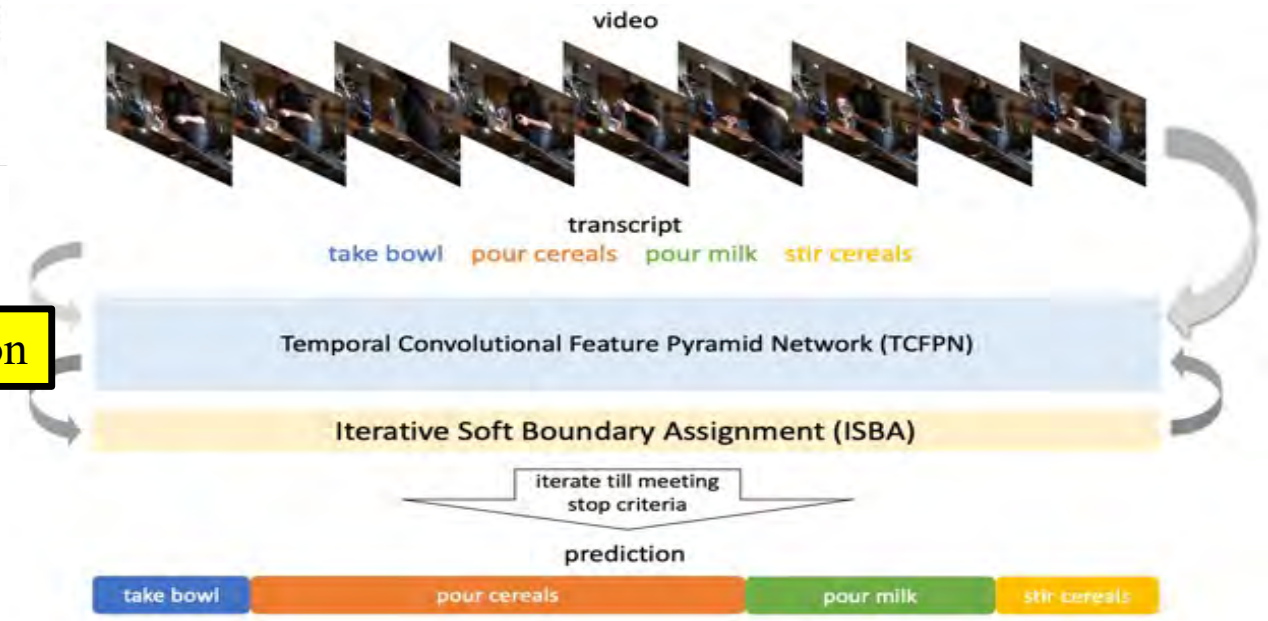


Developing AI-powered models for classification of large XRD data



Static classification

Temporal classification



Current Progress

Total Data Availability:

COD: 476,830 crystal structures

ICSD: 250,343 crystal structures

For Dataset size of 47,049(COD)

Shuffling the data

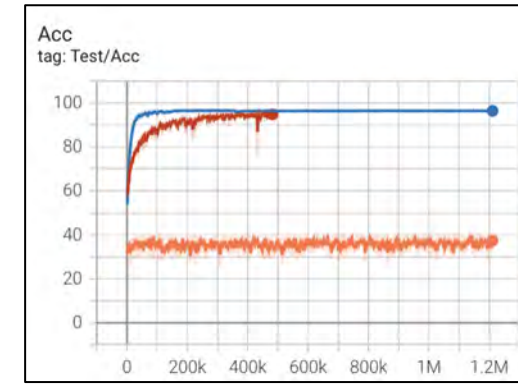
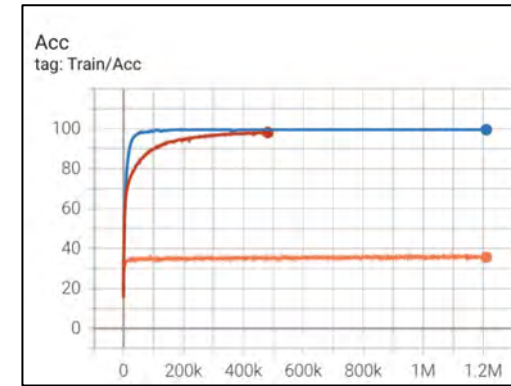
- dividing train/test sets randomly

Accuracy comparison between

- Logistic Regression
- Deep Neural Networks
- Convolutional Neural Network



Classification of 7 crystal systems



For DNN:

While training acc. is 100%

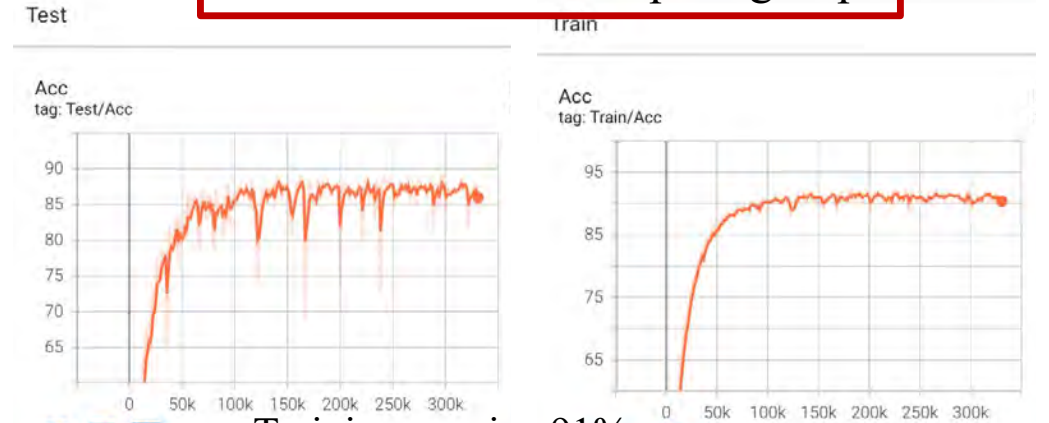
Testing acc. reach **96.42%**

Layer (type)	Output Shape	Param #
Conv1d-1	[-1, 16, 1800]	96
BatchNorm1d-2	[-1, 16, 1800]	32
ReLU-3	[-1, 16, 1800]	0
MaxPool1d-4	[-1, 16, 900]	0
Conv1d-5	[-1, 32, 900]	2,592
BatchNorm1d-6	[-1, 32, 900]	64
ReLU-7	[-1, 32, 900]	0
MaxPool1d-8	[-1, 32, 450]	0
Flatten-9	[-1, 14400]	0
Linear-10	[-1, 7]	100,807

Total params: 103,591
Trainable params: 103,591
Non-trainable params: 0

	0	1	2	3	4	5	6
0	691	24	2	0	0	0	0
1	21	1263	18	1	1	1	1
2	1	38	870	3	2	2	1
3	1	3	5	387	3	1	1
4	0	5	5	1	209	2	1
5	0	2	1	3	3	282	1
6	0	0	1	0	0	0	448

Classification of 230 space groups



Training acc. is ~91%

Testing acc. Reach ~88%

DNN Intermediary architecture

For DNN: Confusion matrix diagonals shows validity

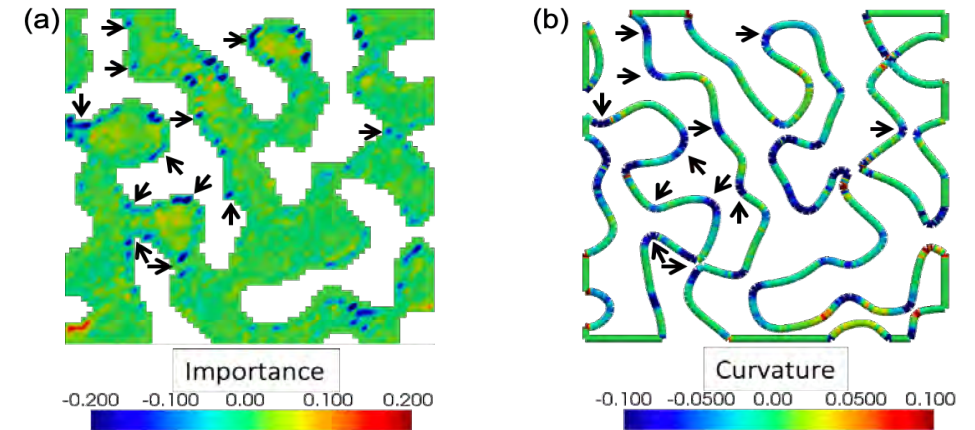
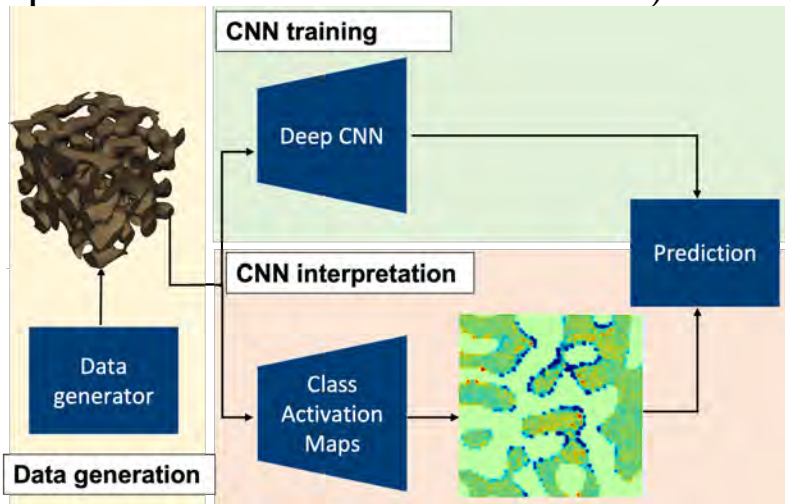


Developing AI-powered models for classification of large XRD data

Interpretation of deep learning models and predictions using explainable deep learning tools, Class Activation Maps (CAMs)

Potential sources of misclassification

- 1) The mixture of phases in the sample
- 2) Lack of XRD patterns in the specific class of training data
- 3) Missing peaks, or too few peaks, present in the XRD pattern
- 4) The peak shifting, broadening, or splitting on time-resolved XRD patterns may be due to various reasons (e.g. multiple plastic deformation mechanisms)

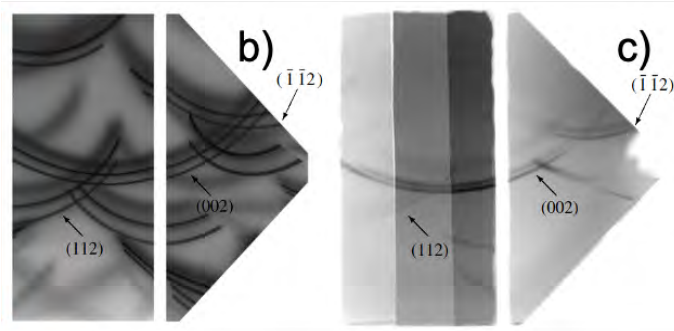


Cross-section of random structure (a) Neuron map of the neuron 38. (b) Gaussian curvature map. Saddle-shaped region is blue. Flat region is green

Mining structure-property linkage in nanoporous materials using an interpretative deep learning approach, *Materialia*, 2022

Developing AI-powered models for classification of large XRD data

Domain adaptation to scarce experimental data



$$\min_{\phi_S, c_S} \mathcal{L}_S(c_S(\phi_S(X_S)), Y_S),$$

$$\phi_T = \mathcal{A}(\phi_S, D_T),$$

$$\min_{c_T} \mathcal{L}_T(c_T(\phi_T(X_T)), Y_T).$$

b) Simulated and (c) experimental film recordings of x-rays diffracted from shock compressed iron

As the NEMD simulations provide direct physical insight into the shock-deformation of materials at the lattice level, and the experimental and simulated time and length scales are converging, it is appropriate to make direct comparisons between the experimentally observed x-ray diffraction signals, and those predicted by the NEMD simulations

G. Kimminau, et al, Simulating picosecond x-ray diffraction from shocked crystals using post-processing molecular dynamics calculations, J. Phys. Condens. Matter. 20 (2008).



Collaborators and acknowledgements

Collaborators:

- Gillbert Collins, UR, LLE
- Russel Hemley, UIC
- Danae Polsin, UR, LLE
- Shuai Zhang, LLE
- Shanti Deemyad, University of Utah
- Saveez Saffarian, University of Utah
- Chenliang Xu, UR
- Hesam Askari, UR

Acknowledge support from:

- DOE
- NSF
- URA
- CIRC

Questions and comments?

niaz@rochester.edu



??

supplementary

Next:

- Machine learning interatomic potentials for complex dynamic processes at high pressures.
- What materials? Na, Mg, Li, Fe
- DFT → MLIP → MD → XRD

Method	Refs.	Regressor	Implementation
Artificial neural networks (Behler)	[40] (2007)	NN	Standalone ("RuNNer"); LAMMPS interface ^[67]
Gaussian approximation potentials (Bartók and Csányi)	[68] (2010)	GPR	GAP code (custom); LAMMPS interface
Spectral neighbor analysis potential (SNAP) (Thompson)	[55,69] (2015)	Linear fit	LAMMPS interface
Adaptive, generalizable, and neighborhood informed (AGNI) force fields (Ramprasad)	[70–72] (2015)	KRR	LAMMPS interface
aenet (Artrith)	[73] (2016)	NN	Standalone ("aenet")
Amp (Korshidi and Peterson)	[74] (2016)	NN	Standalone ("amp"); LAMMPS interface
Moment tensor potentials (Shapeev)	[54,75] (2016)	Linear fit	LAMMPS interface
DeePMD (E)	[76] (2018)	NN	Standalone ("DeePMD-kit"); LAMMPS interface

letters to nature

New high-pressure phases of lithium

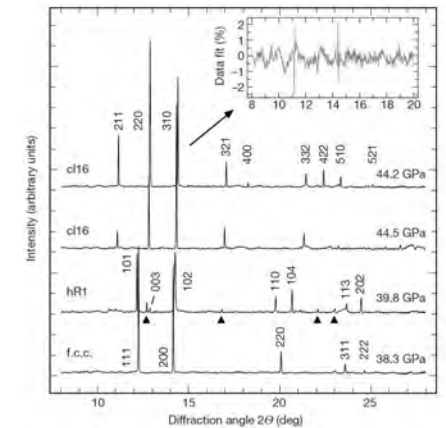
M. Hanfland*, K. Syassen†, N. E. Christensen‡ & D. L. Novikov§

* European Synchrotron Radiation Facility, BP 220, 38043 Grenoble, France

† Max-Planck-Institut für Festkörperforschung, Heisenbergstr. 1, D-70569 Stuttgart, Germany

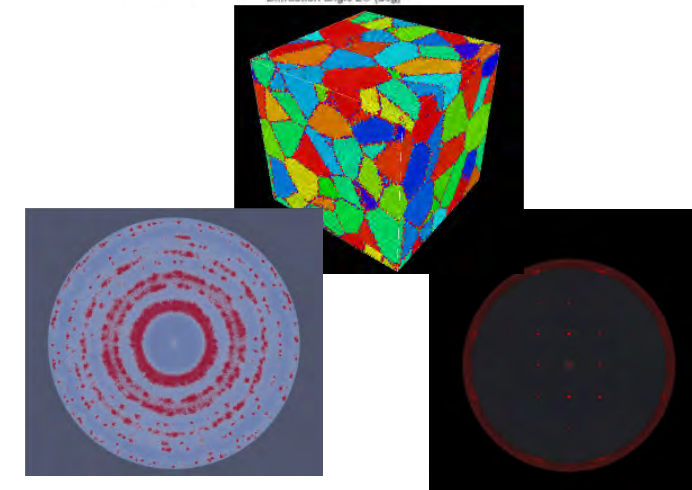
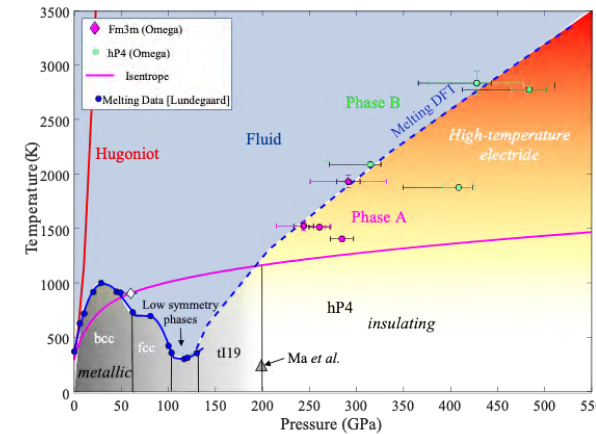
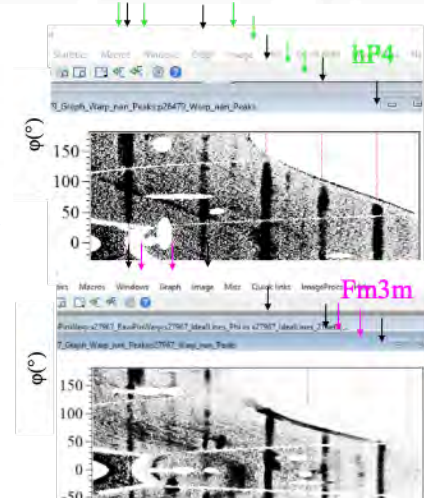
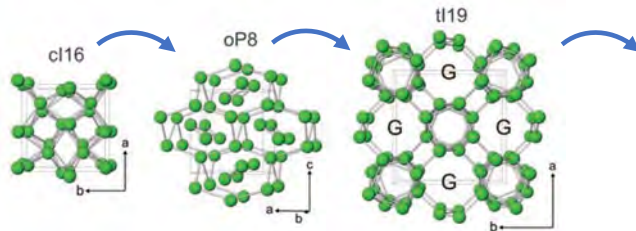
‡ Institute of Physics and Astronomy, Aarhus University, DK-8000 Aarhus C, Denmark

§ Arthur D. Little Inc., Acorn Park, Cambridge, Massachusetts 02140-2390, USA



Structural Diversity of Sodium

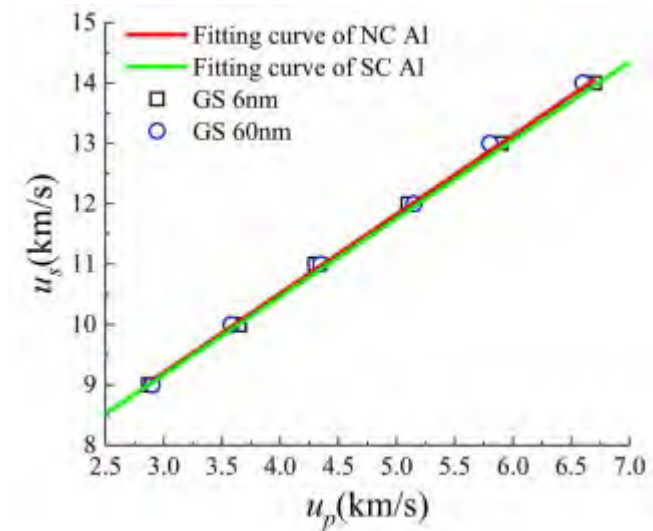
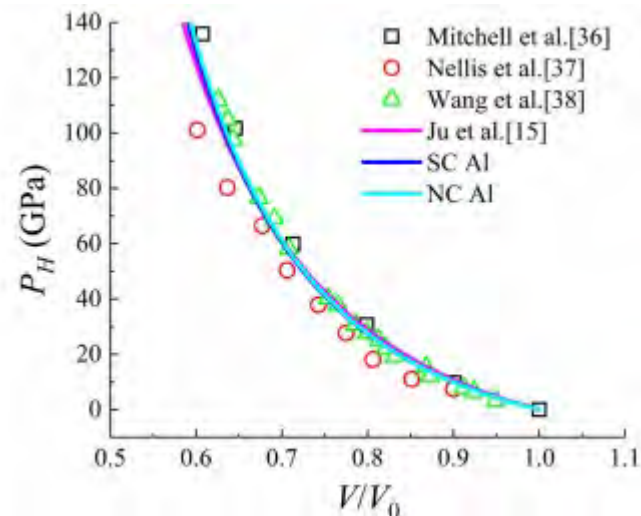
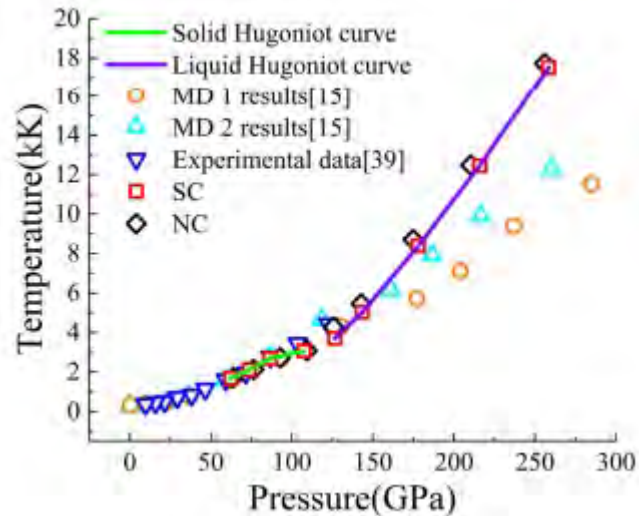
Eugene Gregoryanz,^{1*} Lars F. Lundegaard,¹ Malcolm I. McMahon,¹ Christophe Guillaume,¹ Richard J. Nelmes,¹ Mohamed Mezouar²



Ref: Transforming simple metals to topological insulators: Sodium to 18 Mbars

Texturized nanocrystalline (NC) Al ramp loading

- The interatomic potential we used (developed by Winey et al.**) has also been tested and compared with experiment in terms of Hugoniot curve P_H , Grüneisen coefficient γ and melting temperature T_m at high pressure by Yang et al.** Specifically, they found the linear relation and the Hugoniot curve are almost identical for SC and NC Al and attributed it to because the fact that the grain size cannot nearly affect the dynamic properties of Al at high pressure.



* J. M. Winey. et al., Model. Simul. Mater. Sci. Eng 17, 055004 (2009)

**X. Yang et al., AIP Advances 8, 105212 (2018)